Passive flow control for aerodynamic performance enhancement of airfoil with its application in Wells turbine – Under oscillating flow condition

CrossMark

Ahmed S. Shehata[a,b,*], Qing Xiao[a], Khalid M. Saqr[c], Ahmed Naguib[b], Day Alexander[a]

[a] Department of Naval Architecture, Ocean and Marine Engineering, University of Strathclyde, Glasgow G4 0LZ, UK
[b] Marine Engineering Department, College of Engineering and Technology, Arab Academy for Science Technology and Maritime Transport, P.O. 1029 AbuQir, Alexandria, Egypt
[c] Mechanical Engineering Department, College of Engineering and Technology, Arab Academy for Science Technology and Maritime Transport, P.O. 1029 AbuQir, Alexandria, Egypt

A B S T R A C T

In this work, the passive flow control method was applied to improve the performance of symmetrical airfoil section in the stall regime. In addition to the commonly used first law analysis, the present study utilized an entropy generation minimization method to examine the impact of the flow control method on the entropy generation characteristics around the turbine blade. This work is performed using a time-dependent CFD model of isolated NACA airfoil, which refers to the turbine blade, under sinusoidal flow boundary conditions, which emulates the actual operating conditions. Wells turbine is one of the most proper applications that can be applied by passive flow control method because it is subjected to early stall. Additionally, it consists of a number of blades that have a symmetrical airfoil section subject to the wave condition. It is deduced that with the use of passive flow control, torque coefficient of blade increases by more than 40% within stall regime and by more than 17% before the stall happens. A significantly delayed stall is also observed.

1. Introduction

The techniques developed to maneuver the boundary layer, either for the purpose of increasing the lift or decreasing the drag, are classified under the general heading of boundary layer control or flow control. In order to achieve separation postponement, methods of flow control lift enhancement and drag reduction have been considered. It is important to note that flow control can be defined as a process used to alter a natural flow state or development path (transient between states) into a more desired state (or development path; e.g. laminar, smoother, faster transients) (Collis et al., 2004). Moreover, it could be more precisely defined as modifying the flow field around the airfoil to increase lift and decrease drag. This could be achieved by using different flow control techniques such as blowing and suction, morphing wing, plasma actuators, and changing the shape of the airfoil (Katam, 2005). All the techniques essentially do the same job, i.e. reduce flow separation so that the flow is attached to the airfoil and, thus, reduce drag and increase lift. In regards to flow control techniques, they can be broadly classified as active and passive flow

control which can be further classified into more specific techniques (Gad-el-Hak et al., 1998). The terms "active" or "passive" do not have any clearly accepted definitions, but nonetheless are frequently used. Typically, the classification is based on energy addition, either on the possibility of finding parameters and modifying them after the system is built, or on the steadiness of the control system; whether it is steady or unsteady. Such studies have demonstrated that suction slot can modify the pressure distribution over an airfoil surface and have a substantial effect on lift and drag coefficients (Yousefi et al., 2014; Chapin and Benard, 2015; Schatz et al., 2007; Chawla et al., 2014; Fernandez et al., 2013; Volino et al., 2011). A wide variety of different studies have been conducted on flow control techniques. In actual fact, in 1904, Prandtl (Schlichting, 1968) was the first scientist who employed boundary layer suction on a cylindrical surface to delay boundary layer separation. The earliest known experimental works on boundary layer suction for wings were conducted in the late 1930s and the 1940s (Richards and Burge, 1943; Walker and Raymer, 1946; Braslow, 1999). Huang et al. (2004) studied the suction and blowing flow control techniques on a NACA0012 airfoil. The combination of jet

---

Nomenclature

A	The total blade area (m^2)	S_t	Thermal entropy generation rate (W/m^2 K)
c	Blade chord (m)	S_V	Viscous entropy generation rate (W/m^2 K)
C_D	Drag force coefficient	T_o	Reservoir temperature (K)
C_L	Lift force coefficient	U	Moving frame velocity (m/s)
C_T	Torque coefficient	$\bar{u}_i$	Reynolds Averaged velocity component in i direction (m/s)
D	The fluid domain		
D_{ss}	Suction slot diameter (m)	V	Volume of a computation cell (m^3)
f	Cycle frequency (Hz)	V_a	Instantaneous Velocity (m/s)
F_D	In-line force acting on cylinder (N)	V_{am}	Highest speed of axial direction (m/s)
G	The filter function	V_o	Initial velocity for computation (m/s)
KE	Kinetic Energy (J)	V_r	Relative velocity (m/s)
L_{ss}	Suction slot location from leading edge in chord percentage %	$\dot{W}$	The net-work transfer rate (W/s)
		$\dot{W}_{rev}$	Reversible work transfer rate (W/s)
K	Turbulent kinetic energy (J/kg)	η_F	The efficiency in first law of thermodynamics
Δp	Pressure difference across the turbine (N/m^2)	η_S	The second law efficiency
R_m	Mean rotor radius (m)	μ	Viscosity (kg/m s)
S_{gen}	Local entropy generation rate (W/m^2 K)	μ_t	Turbulent viscosity (N s/m^2)
S_G	Global entropy generation rate (W/K)	ρ	Density (kg/m^3)
S_{ij}	Mean strain rate (1/s)	$\overline{\varnothing}$	Flow coefficient
		ω	Rotor angular speed (rad/s)
		$(-\overline{\rho u_i' u_j'})$	Reynolds stress tensor

location and angle of attack showed a remarkable difference concerning lift coefficient as perpendicular suction at the leading edge increased in comparison to the case in other suction situations. Moreover, the tangential blowing at downstream locations was found to lead to the maximum increase in the lift coefficient value. Rosas (2005) numerically studied flow separation control through oscillatory fluid injection, in which lift coefficient increased. The authors in Akcayoz and Tuncer (2009) examined the optimization of synthetic jet parameters on a NACA0015 airfoil in different angles of attack to increase the lift to drag ratio. Their results revealed that the optimum jet location moved toward the leading edge and the optimum jet angle incremented as the angle of attack increased. The CFD method has been increasingly used to investigate boundary layer control. Many flow control studies by CFD approaches (Kim and Kim, 2009; Genc et al., 2011; Rumsey and Nishino, 2011; Yagiz et al., 2012) have been conducted to investigate the effects of blowing and suction jets on the aerodynamic performance of airfoils.

The major challenge facing oscillating water column ocean energy extraction systems is to find an efficient and economical means of converting flow kinetic energy to unidirectional rotary motion for driving electrical generators (Rosa, 2012; Curran and Folley, 2008; Falcao, 1999, 2004; Torres et al., 2016), as seen in Fig. 1. The energy conversion from the oscillating air column (Boccotti, 2007a, 2007b) can be achieved by using a self-rectifying air turbine such as Wells turbine which was invented by Wells in 1976, see Fig. 2 (Raghunathan, 1980; Hitoshi Hotta, 1985; Masahiro Inoue et al., 1985; Masami Suzuki and Tagori, 1985; Yukihisa Washio et al., 1985; Folley et al., 2006). Wells turbine consists of a number of blades that have symmetrical airfoil section. This airfoil section under different conditions with various geometric parameters was investigated by other researchers in consideration of improving the overall system performance. In order to achieve this purpose, different methods were used, such as experimental, analytical and numerical simulation. The main disadvantage of Wells turbine is the stall condition (Shehata et al., 2017b). Aerodynamic bodies subjected to pitching motions or oscillations exhibit a stalling behavior different from that observed when the flow over a wing at a fixed angle of attack separates. The latter phenomenon is referred to as static stall, since the angle of attack is fixed. In the case of a dynamically pitching body, such as an airfoil with large flow rates and a large angle of attack, the shear layer near the leading edge rolls up to form a leading-edge vortex which provides additional suction over the upper airfoil surface as it convects down-

stream. This increased suction leads to performance gains in lift and stall delay, but the leading-edge vortex quickly becomes unstable and detaches from the airfoil. As soon as it passes behind the trailing edge, however, the leading-edge vortex detachment is accompanied by a dramatic decrease in lift and a significant increase in drag. This phenomenon is called dynamic stall. From Fig. 3 it can be noted that Wells turbine can extract power at low air flow rate, when other turbines would be inefficient (Liu et al., 2016; Okuhara et al., 2013). Also, the aerodynamic efficiency increases with the increase of the flow coefficient (angle of attack) up to a certain value, after which it decreases. Thus, most of the past studies aimed to 1) improve the torque coefficient (the turbine output) and 2) improve the turbine behavior under the stall condition. In a number of previous studies (Raghunathan, 1995a; Dixon, 1998; Sheldahl and Klimas, 1981), it was concluded that the delay of stall onset contributes to improving Wells turbine performance. This delay can be achieved by setting guide vanes on the rotor's hub (Raghunathan, 1995a, 1995b; Brito-Melo et al., 2002). It was found that a multi-plane turbine without guide vanes was less efficient (approximately 20%) than the one with guide vanes. A comparison between Wells turbines having 2D guide vanes and 3D guide vanes was investigated (Setoguchi et al., 2001; Takao et al., 2001) by testing a Wells turbine model under steady flow conditions, and using the computer simulation (quasi-steady analysis. It demonstrated that, the 3D case has superior characteristics in the running and starting characteristics. Concerning Wells turbine systems which
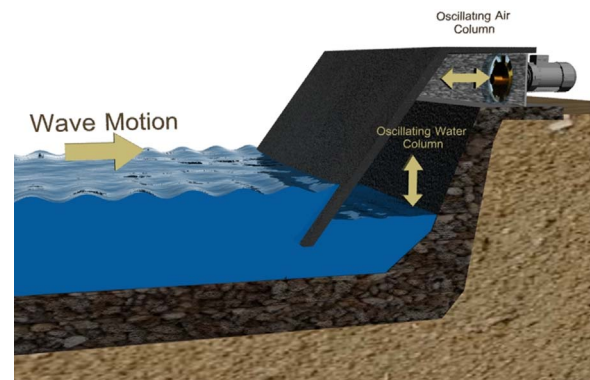
Fig. 1. An illustration of the principle of operation of OWC system, where the wave motion is used to drive a turbine through the oscillation of air column (Takao et al., 2001).
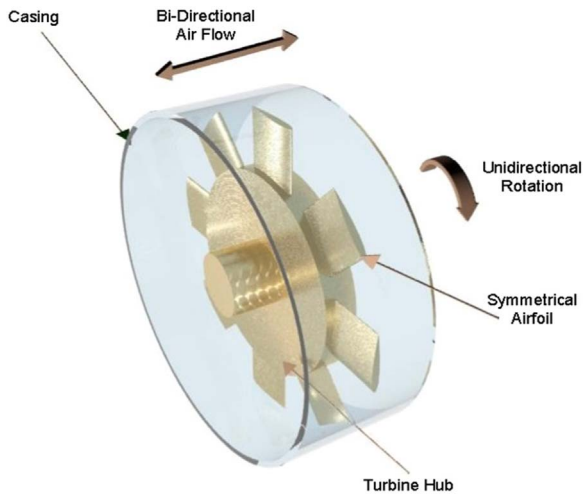
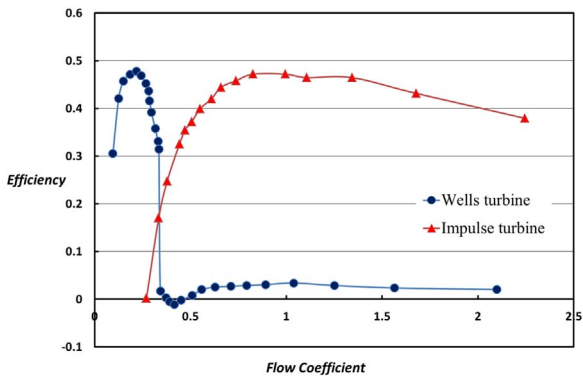**Fig. 2.** Typical structure of Wells turbine rotor (Takao et al., 2001).

Fig. 3. Turbines characteristic under steady flow conditions: Flow coefficient variation with the efficiency (Akcayoz and Tuncer, 2009).
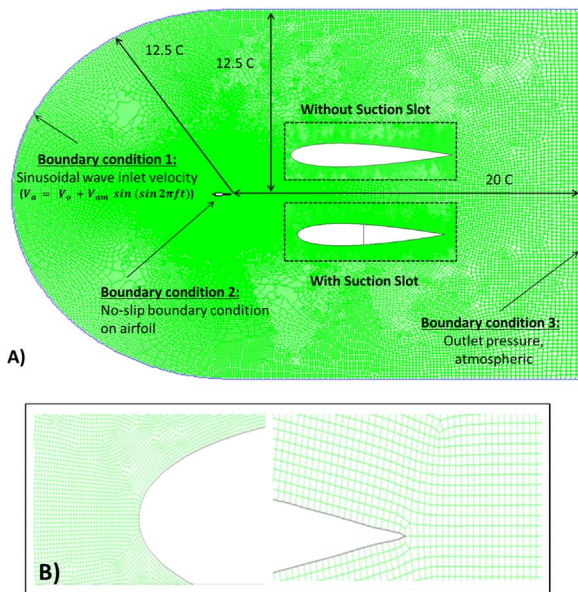

Fig. 4. Computational model and boundary conditions A) dimensions of whole computational domain and location of airfoil B) computational grid near the wall of the airfoil.

operate at high pressure values, a multi plane (usually tow stage) turbine configuration can be used. Such a concept avoids the use of guide vanes and, therefore, the turbine would require less maintenance and repairs (Raghunathan, 1995a). The performance of a biplane Wells
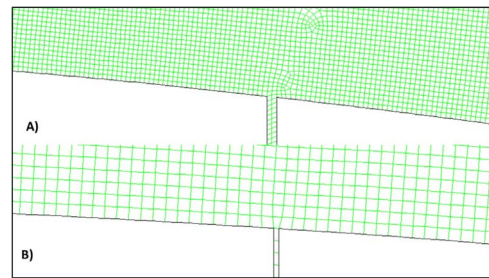

Fig. 5. The near views of slot mesh A) D_{SS}=0.005 m B) D_{SS}=0.001 m.

turbine is dependent on the gap between the planes as it is shown in Raghunathan (1995a). A gap-to-chord ratio between the planes of 1.0 was recommended. Experimental results in Gato and Curran (1996) showed that the use of two twin rotors rotating in the opposite direction to each other was an efficient means of recovering the swirl kinetic energy without the use of guide vanes. The overall performance of several types of Wells turbine design have been investigated in Raghunathan and Beattie (1996) and, a semi-empirical method for predicting the performance has been used in Curran et al. (1998). Similar comparisons were undertaken using experimental measurement in Gato and Curran (1997). It can be observed that the contra-rotating turbine had an operational range which was similar to that of the monoplane turbine with guide vanes and it achieved similar peak efficiency as well. However, the flow performed was better than the latter in the post-stall regime. In order to improve the performance of the Wells turbine, the effect of end plate on the turbine characteristics has been investigated in Mamun et al. (2006), Takao et al. (2007). Using an experimental model and a CFD method it was shown that the optimum plate position was a forward type. The peak efficiency increases approximately 4% as compared to the Wells turbine without an endplate. The calculations of the blade sweeps for the Wells turbine with a numerical code by Kim et al. (2002) and experimentally with quasi-steady analysis in Setoguchi et al. (2003a). As a result, it was concluded that the performance of the Wells turbines was influenced by the blade sweep area.

Exergy analysis is performed using the numerical simulation for steady state biplane Wells turbines (Shaaban, 2012) where the upstream rotor has a design point second law efficiency of 82.3% although the downstream rotor second law efficiency equals 60.7%. The entropy generation, due to viscous dissipation, around different 2D airfoil sections for Wells turbine was recently examined by the authors in Shehata et al. (2014, 2016). When Reynolds number was increased from 6×10^4 to 1×10^5 the total entropy generation increased more than two folds for both airfoils correspondingly. However, when Reynolds number was increased further to 2×10^5, the total entropy generation exhibited unintuitive values ranging from 25% less to 20% higher than the corresponding value at Reynolds number=1×10^5. The efficiency for four different airfoils in the compression cycle is higher than the suction cycle at 2° angle of attack. Although, when the angle of attack increases, the efficiency for the suction cycle increases much more than the compression one. This study suggested that a possible existence of critical Reynolds number for the operating condition at which viscous irreversibilities takes minimum values. A comparison between total entropy generation of a suggested design (with variable chord) and a constant chord of Wells turbine was presented in Soltanmohamadi and Lakzian (2015). The detailed results demonstrate an increase in static pressure difference around a new blade and a 26.02% average decrease in total entropy generation throughout the full operating range. Most of the researchers studied the performance of different airfoils design and different operational conditions where analyzing the problem was only based on the parameter of first law of thermodynamics. In order to form a deeper understanding, it is necessary to look at the second law of thermodynamics since it has shown very promising result in many
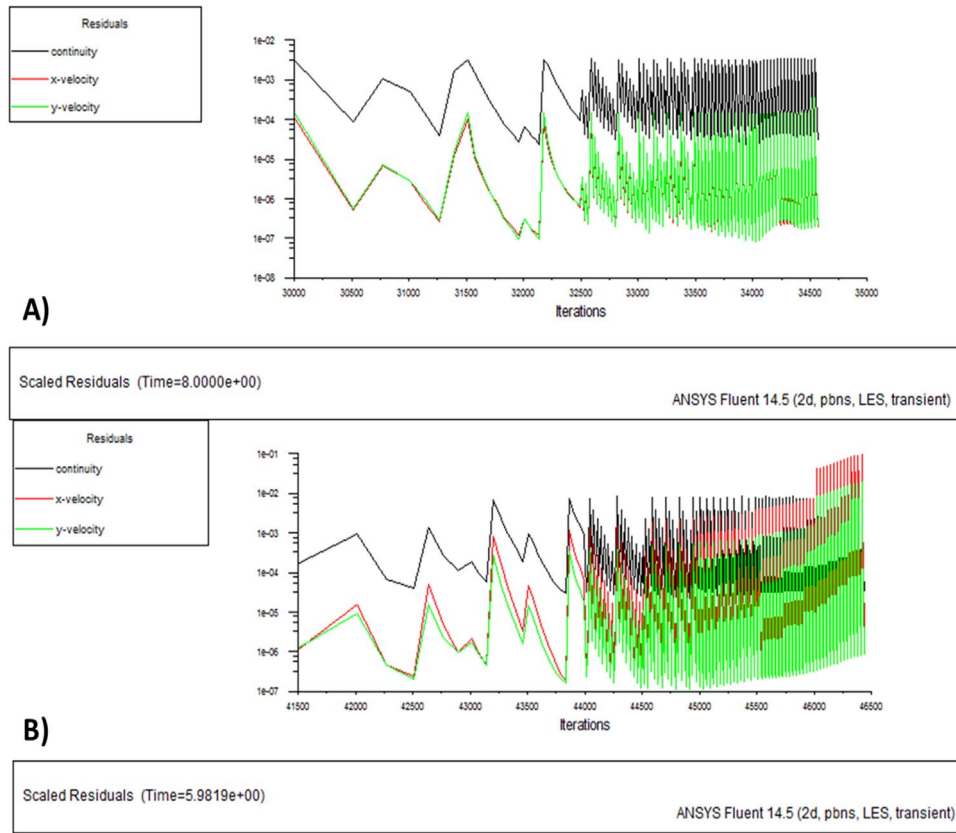
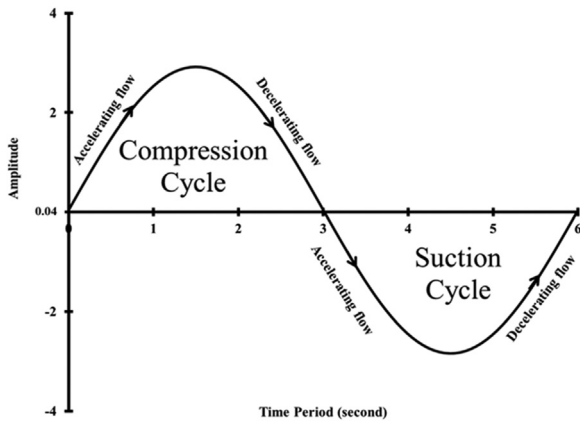Fig. 6. Convergence criteria A) non-oscillating flow B) sinusoidal flow.

Fig. 7. The sinusoidal wave boundary condition, which represents a regular oscillating water column.
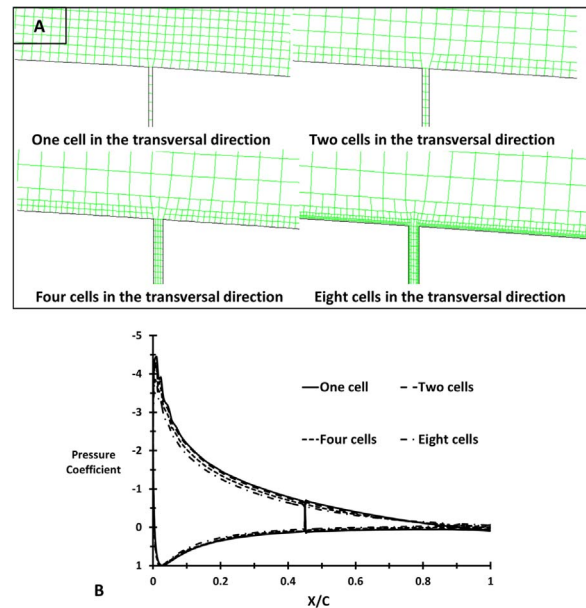

Fig. 8. A grid sensitivity analysis with respect to cell number across the slot section A) one, two, four and eight cells in the transversal direction B) pressure coefficient plotted on the normalized aerofoil cord at different grid resolutions.

applications, such as wind turbine in Pope et al. (2010), Baskut et al. (2010, 2011), Redha et al. (2011), Ozgener and Ozgener (2007), Mortazavi et al. (2015), and gas turbine in Şöhret et al. (2015), Ghazikhani et al. (2014), Sue and Chuang (2004), Kim and Kim (2012), Jubeh (2005), Lugo-Leyte et al. (2015).

Wells turbine consists of a number of blades that have symmetrical airfoil section. This airfoil section under different conditions with various geometric parameters was investigated by other researchers to improve the overall system performance. Different methods were used to achieve this purpose, such as experimental, analytical and numerical simulation. In this work the CFD analysis is used to investigate and analyze the flow around the isolated NACA airfoil, which refers to the turbine blade, under sinusoidal flow boundary conditions, which emulates the actual operating conditions. The force coefficients, such as torque coefficient and the entropy generation

value, are calculated and compared under different conditions with various design parameters by analyzing the flow around the airfoil section using CFD software, where the force coefficients are referring to the first law analysis and the entropy generation value is referring to the second law analysis. The objective of the present work is to demonstrate that the performance of airfoil section, which refers to the Wells turbine blade at stall and near-stall conditions, can be radically improved by using passive flow control method such as
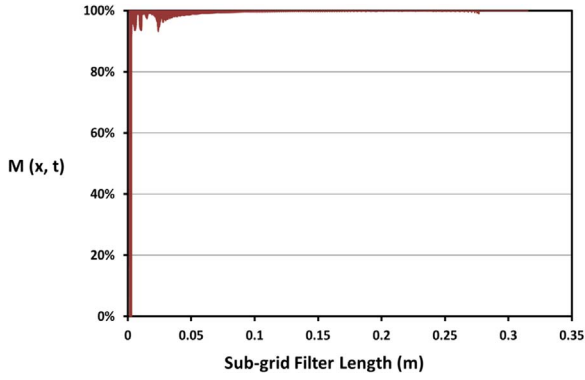
Fig. 9. The measure of LES quality by M(x, t) with the sub-grid filter length.
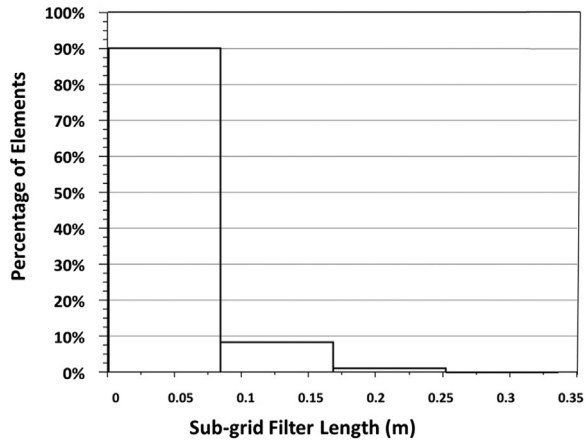

Fig. 10. A histogram of number of elements for the sub-grid filter length.

suction or blowing slot. Therefore, a typical slot is created in the airfoil section, normal to the chord, and due to the pressure difference between the two surfaces. Consequently, a suction effect occurs which delays the stall. Accordingly, there is no need to generate any specific active suction or blowing within the airfoil or the slot. Along with this design, there are two new aspects here. The first is improving the performance of airfoil section for Wells turbine in near-stall conditions. The second is to study the effect of slot in oscillating (i.e. sinusoidal) flow, which is newly compared to the unidirectional flow as in aerodynamics applications. Apart from that, an entropy generation minimization method is used to conduct the second-law analysis as recently reported by the authors in Shehata et al. (2014, 2016). An investigation on the entropy generation, due to viscous dissipation, around turbine airfoils in two-dimensional unsteady flow configurations, will be carried out. In reference to the literature, no specific unsteady CFD study of the slot effect with sinusoidal flow on the entropy generation rate has been performed for airfoil section of Wells turbine.

2. Mathematical model and numerical approach

The governing equations employed for Large Eddy Simulation (LES) are obtained by filtering the time-dependent Navier-Stokes equations. The filtering process effectively filters out eddies whose scales are smaller than the filter width or grid spacing used in the computations. The resulting equations thus govern the dynamics of large eddies. A filtered variable (denoted by an over-bar) is defined by SB (2000):

$$\overline{\phi}(x) = \int_D \phi(x') G(x, x') dx' \qquad (1)$$

where D is the fluid domain, and G is the filter function that determines

the scale of the resolved eddies. In FLUENT, the finite-volume discretization itself implicitly provides the filtering operation (Mamun, 2006):

$$\overline{\phi}(x) = \frac{1}{V} \int_V \phi(x') dx', \ x' \in V \qquad (2)$$

where V is the volume of a computational cell. The filter function, G (x, x′), implied here is then

$$G(x, x') = \begin{cases} 1/V & for \ x' \in V \\ 0 & otherwise \end{cases} \qquad (3)$$

The LES model will be applied to essentially incompressible (but not necessarily constant-density) flows. By filtering the incompressible Navier-Stokes equations, one obtains (Dahlstrom, 2003)

$$\frac{\partial \rho}{\partial t} + \frac{\partial \rho \overline{u}_i}{\partial x_i} = 0 \qquad (4)$$

$$\frac{\partial}{\partial t}(\rho \overline{u}_i) + \frac{\partial}{\partial x_j}(\rho \overline{u}_i \overline{u}_j) = \frac{\partial}{\partial x_j}\left(\mu \frac{\partial \overline{u}_i}{\partial x_j}\right) - \frac{\partial \overline{p}}{\partial x_i} - \frac{\partial \tau_{ij}}{\partial x_j} \qquad (5)$$

where τ_{ij} is the sub-grid-scale stress defined by

$$\tau_{ij} = \rho \overline{u_i u_j} - \rho \overline{u}_i \overline{u}_j \qquad (6)$$

The sub-grid-scale stresses resulting from the filtering operation are unidentified, and require modeling. The majority of sub-grid-scale models are eddy viscosity models of the following form (Moin et al., 1991):

$$\tau_{ij} - \frac{1}{3}\tau_{kk}\sigma_{ij} = -2\mu_t \overline{S}_{ij} \qquad (7)$$

where $\overline{S}_{ij}$ is the rate-of-strain tensor for the resolved scale defined by:

$$\overline{S}_{ij} = \frac{1}{2}\left(\frac{\partial \overline{u}_i}{\partial x_j} + \frac{\partial \overline{u}_j}{\partial x_i}\right) \qquad (8)$$

and μ_t is the sub-grid-scale turbulent viscosity, which the Smagorinsky-Lilly model is used for it (DK, 1992). The most basic of sub-grid-scale models for "Smagorinsky-Lilly model" was proposed by Smagorinsky (Hinze, 1975) and was further developed by Lilly (Launder and Spalding, 1972). In the Smagorinsky-Lilly model, the eddy viscosity is modeled by:

$$\mu_t = \rho L_s^2 |\overline{S}| \qquad (9)$$

where L_s is the mixing length for sub-grid-scale models and $|\overline{S}| = \sqrt{2\overline{S}_{ij}\overline{S}_{ij}}$. The L_s is computed using:

$$L_s = \min \ (kd, \quad C_s V^{1/3}) \qquad (10)$$

where C_s is the Smagorinsky constant, $k = 0.42$, d is the distance to the closest wall, and V is the volume of the computational cell. Lilly derived a value of 0.23 for C_s from homogeneous isotropic turbulence. However, this value was found to cause excessive damping of large-scale fluctuations in the presence of mean shear or in transitional flows. C_s=0.1 has been found to yield the best results for a wide range of flows.

For the first law of thermodynamics, the lift and drag coefficient C_L and C_D are computed from the post processing software. The average value for lift and drag coefficient was used to calculate one value for torque coefficient for each angle of attack. Afterwards, the torque coefficient can then be expressed as (Sheldahl and Klimas, 1981; Curran et al., 1998; Whittaker et al., 1997):

$$C_T = (C_L sin\alpha - C_D \cos\alpha) \qquad (11)$$

The flow coefficient $\overline{\phi}$ relating tangential and axial velocities of the rotor is defined as

$$\overline{\phi} = \frac{V_a}{\omega * R_m} \qquad (12)$$

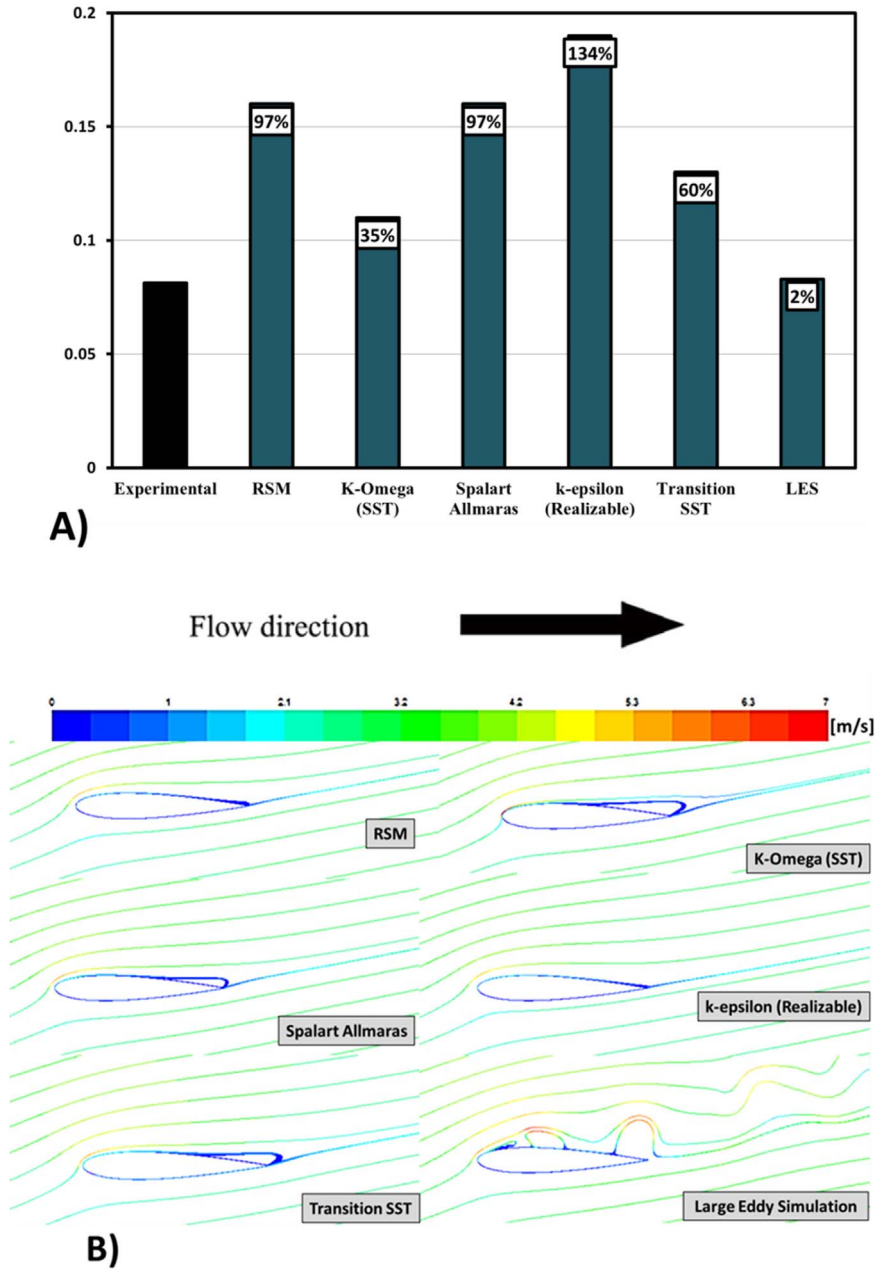where the α angle of attack equal to

Fig. 11. Comparison between different models to simulate the stall angle from experimental data A) torque coefficient B) path-line colored by the velocity magnitude C) contours of pressure distribution D) pressure distribution at upper and lower surface. (For interpretation of the references to color in this figure legend, the reader is referred to the web version of this article.)

$$\alpha = tan^{-1} \frac{V_a}{\omega R_m} \tag{13}$$

and the torque as:

$$Torque = \frac{1}{2}\rho \left(V_a{}^2 + (\omega R_m)^2\right) A R_m C_T \tag{14}$$

the efficiency in the first law of thermodynamics (η_F) is defined as:

$$\eta_F = \frac{Torque^* \quad \omega}{\Delta P^* Q} \tag{15}$$

The transport equations of such models can be found in turbulence modeling texts such as Hirsch (2007). The second law of thermodynamic defines the network transfer rate $\dot{W}$ as Bejan (1996):

$$\dot{W}_{rev} - \dot{W} = T_o S_{gen} \tag{16}$$

Which has been known for most of this century in engineering as

the Gouy–Stodola theorem (Stodola, 1910).

It is possible to express the irreversible entropy generation in terms of the derivatives of local flow quantities in the absence of phase changes and chemical reactions. The two dissipative mechanisms in viscous flow are the strain-originated dissipation and the thermal dissipation which correspond to a viscous and a thermal entropy generation respectively (Iandoli, 2005). Thus, it can be written,

$$S_{gen} = S_V + S_{th} \tag{17}$$

In incompressible isothermal flow, such as the case in hand, the thermal dissipation term vanishes. The local viscous irreversibilities therefore can be expressed as:

$$S_V = \frac{\mu}{T_o}\phi \tag{18}$$

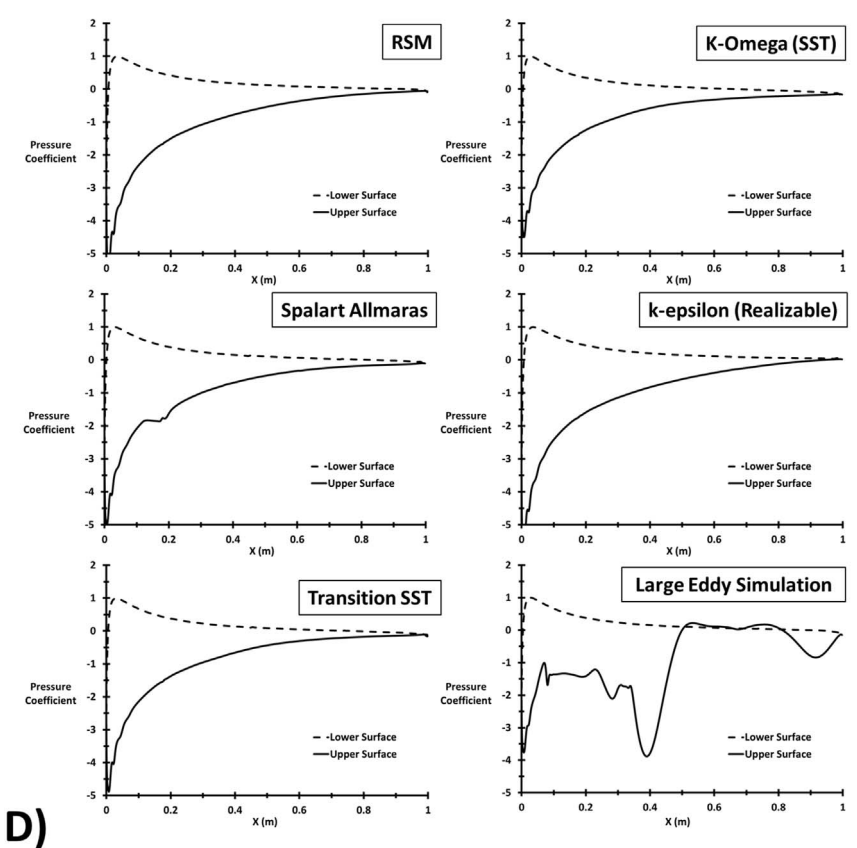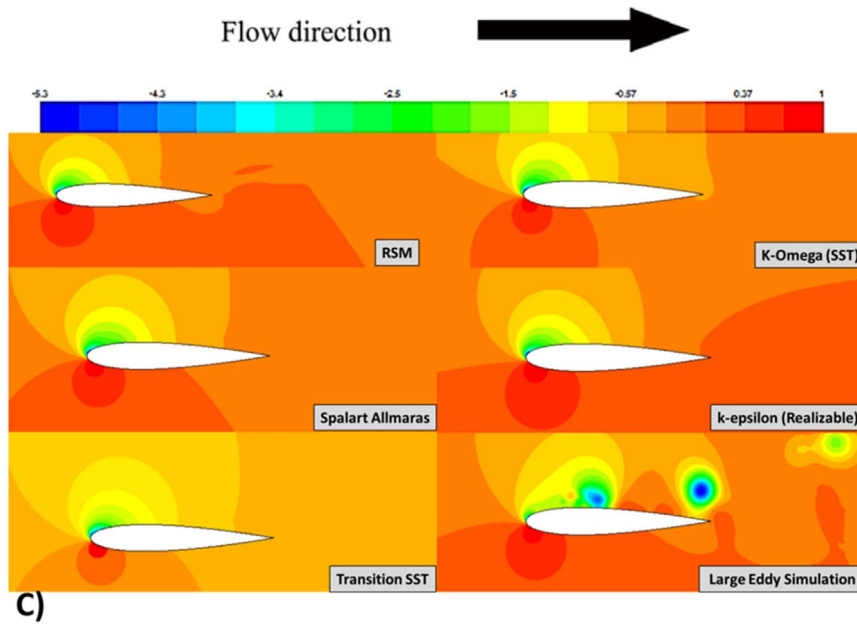where ϕ is the viscous dissipation term, that is expressed in two

Flow direction

Fig. 11. (*continued*)

dimensional Cartesian coordinates as Iandoli (2005):

$$\phi = 2\left[\left(\frac{\partial u}{\partial x}\right)^2 + \left(\frac{\partial v}{\partial y}\right)^2\right] + \left(\frac{\partial u}{\partial y} + \frac{\partial v}{\partial x}\right)^2 \tag{19}$$

Eqs. (18) and (19) were used to create the UDF file, which is used to calculate the local entropy form the FLUENT software. Then, the global entropy generation rate is hence expressed as:

$$S_G = \iint_{xy} S_V \, dy \, dx \tag{20}$$

Which is also calculated from the FLUENT software by integral the global value,

The next equation is defining the exergy value, which can be written as Bejan (1995):

$$Exergy = KE + S_G \tag{21}$$

and finally the second law efficiency is defined as Pope et al. (2010):

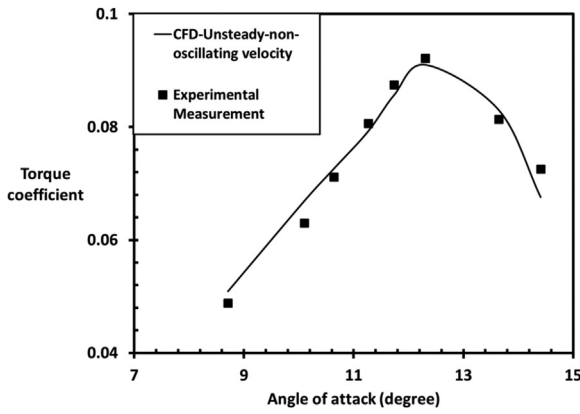$$\eta_S = \frac{KE}{Exergy} \tag{22}$$

Fig. 12. Measured torque coefficient from Refs. Torresi et al. (2007b, 2007a, 2009) and calculated torque coefficient from present CFD unsteady flow with non-oscillating velocity.

where $KE = \frac{1}{2}V^2$

From the above equation we can come up with a number of conclusions. On the one hand, that the torque coefficient indicates to the first law efficiency and the global entropy generation rate indicates to the second law and efficiency, in which the increase in torque coefficient leads to increase in the first law efficiency. On the other hand, the decrease in the global entropy generation rate leads to an increase in the second law efficiency.

3. CFD approach

3.1. Computational model, solver details and boundary conditions

Two-dimensional numerical models for NACA0015 airfoils were built and validated against experimental measurements under unsteady flow conditions with both non-oscillating velocity, and sinusoidal inlet velocity. The computational domain is discretized to Cartesian structured finite volume cells using GAMBIT code. The application of such boundary condition types (Starzmann and Carolus, 2013; Mohamed and Shaaban, 2013; Torresi et al., 2009; Mamun et al., 2004) matches the Green-Gauss cell based evaluation method for the gradient terms used in the solver (ANSYS FLUENT). Numerous tests accounting for different interpolation schemes were used to compute cell face values of the flow field variables. The variables of governing equation which are velocity and pressure, as well as convergence tests have been undertaken. The second order upwind (Smagorinsky, 1963) interpolation scheme was used in this work in which it yields results which are approximately similar to such yielded by third order MUSCL scheme in the present situation. In addition, in some cases of the third order MUSCL scheme was given high oscillatory residual during the solution. Fig. 4 demonstrates the dimensions of the whole computational domain and the location of airfoil, and it also shows the grid distribution near the wall of the airfoil. Furthermore, the near views of slot mesh can be determined from Fig. 5 for different slot diameter. The Quad-Pave meshing scheme (Structured Grid) is used in this work. It

Fig. 13. Measured unsteady in-line force F_D from Ref. Nomura et al. (2003), (angle of attack=0°) and F_D calculated from the present CFD for frequency 2 Hz.

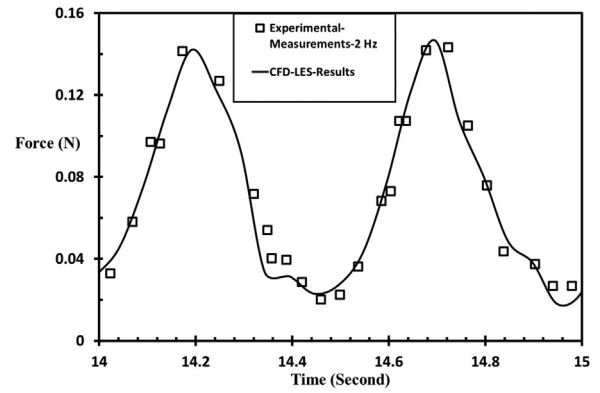**Fig. 14.** Measured unsteady in-line force F_D from Ref. Nomura et al. (2003), (angle of attack=0°) and F_D calculated from the present CFD for frequency 1 Hz.
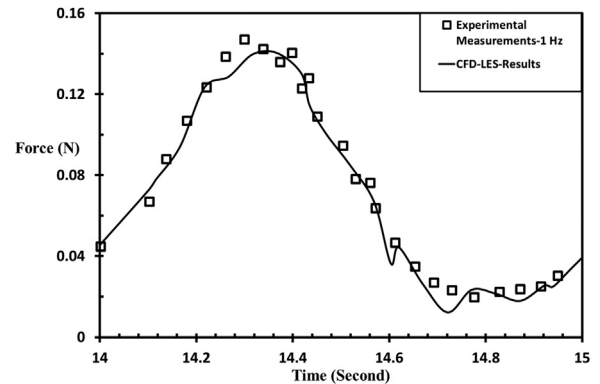
was also detected that the solution reaches convergence when the scaled residuals approaches 1×10^{-5}. See Fig. 6 for the convergence criteria in the non-oscillating flow and sinusoidal flow inlet velocity. At such limit, the flow field variables holds constant values with the application of consecutive iterations.

The axial flow of Wells Turbine is modeled as a sinusoidal wave in this simulation. Therefore, Inlet boundary conditions are set to change as time. In order to apply the inlet boundary condition, inlet velocity with periodic function (see Fig. 7) is generated as follows.

$$V_a = V_o + V_{am} sin(\sin 2\pi ft) \qquad (23)$$

Where t is time period, 6 s are set as one period in this simulation considering to the literature survey (Mamun et al., 2004; Setoguchi et al., 2003b; Kinoue et al., 2003a, 2004). Time step is set as 0.000296721 s in order to satisfy CFL (Courant Friedrichs Lewy) (DE Moura and Carlos, 2013) condition equal to 1. The sinusoidal wave condition create various Reynolds number up to 2×10^4 according to the Ref. Torresi et al. (2009).

Table 1
The error percentage between measured torque coefficient from Refs. Torresi et al. (2007b, 2007a, 2009) and calculated torque coefficient from CFD under unsteady flow with non-oscillating velocity.

Torque Coefficient	Angle of attack (Degree)							
	8.709	10.097	10.639	11.266	11.734	12.304	13.642	14.406
Experimental	0.0488	0.0631	0.0712	0.0807	0.0875	0.0922	0.0814	0.0725
CFD	0.05092	0.06689	0.0726	0.0793	0.0856	0.091	0.083	0.0676
Error %	4	6	2	−2	−2	−1	2	−7

Table 2

The error percentage between measured F_D from Ref. Nomura et al. (2003) and calculated F_D from CFD under unsteady flow with sinusoidal inlet velocity.

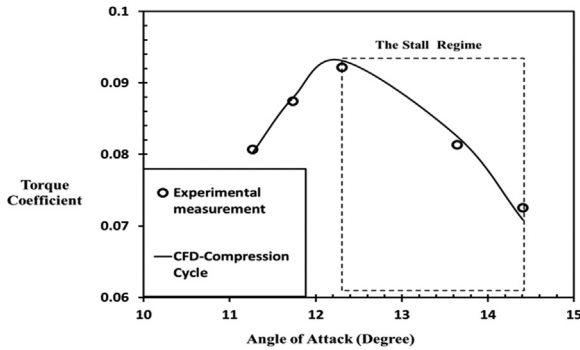| F_D*10^{-2} (N)	Time (s)												
	14.02	14.1	14.12	14.2	14.3	14.34	14.4	14.5	14.6	14.7	14.8	14.9	15
Frequency 2 Hz													
Experimental	3.3	7.6	9.7	14.1	12.7	3.3	4	2.3	7.4	14.4	10.5	3.8	2.6
CFD	3.7	7.6	9.6	14.2	12.3	3.4	3.3	2.6	7.6	14.6	10.7	3.7	2.4
Error %	11	1	−1	1	−4	1	−17	17	4	1	2	−2	−11
Frequency 1 Hz													
Experimental	4.4	6.8	12.4	13.8	14	12.7	10	7.6	4.6	2.7	2.3	2.5	2.9
CFD	4.5	7.1	12.4	12.9	14	12.9	10.1	8.4	4.4	2.6	2.2	2.6	3.2
Error %	2	4	0	−7	0	1	1	10	−4	1	−4	4	10

Fig. 15. Measured torque coefficient from Refs. Torresi et al. (2007b, 2007a, 2009) and calculated torque coefficient from CFD unsteady flow with sinusoidal inlet velocity.

Table 3

The error percentage between measured torque coefficient from Refs. Torresi et al. (2007b, 2007a, 2009) and calculated torque coefficient from CFD under unsteady flow with sinusoidal inlet velocity.

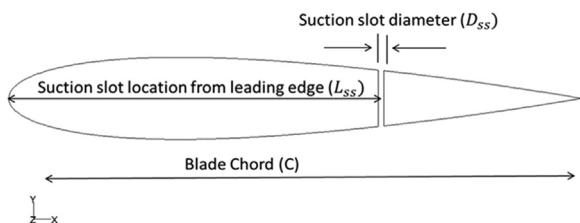| Torque Coefficient	Angle of attack (Degree)				
	11.266	11.734	12.304	13.642	14.406
Experimental	0.0807	0.0875	0.092	0.0814	0.0725
CFD	0.0803	0.0879	0.0931	0.0825	0.0709
Error %	−1	1	1	1	−2

Fig. 16. 2D airfoil diagram with a slot.

3.2. Grid sensitivity test

In order to ensure that the numerical produces results are minimally dependent on the grid size, several grids were tested to estimate the number of grid cells required to establish a reliable model. The grid sensitivity test is performed where 4 grids with different mesh sizes ranging from 112603 up to 446889 cells are investigated. This test shows that for grids with mesh sizes of 312951 cells, gives good result within reasonable computation time (more details about this result in Shehata et al. (2014)). Therefore, it was selected to conduct the analysis presented hereafter.

Fig. 8 show the grid sensitivity analysis with respect to cell number across the slot section for one, two, four and eight cells in the transversal direction. It can be noted that the results for the four grids A–D are approximately the same. On the other hand, by increase the number of cells in the transversal direction, the cells number for the total domain is increase for the four grids A–D by 312951, 350662, 388637 and 413665 respectively. Therefore, the grid A was selected in order to immunize the solution time of the different cases without impacting on the quality and accuracy of the results.

3.3. LES resolution quality assessment

In the most common practice, in LES, the filter length depends on the resolution of spatial discretization (i.e. grid) in a specified problem. The implication of the filtering technique, which is the backbone of LES, is the question about the resolution of the resolved scales in comparison with the total turbulence spectrum in the flow. An assortment of several attempts were made to propose and index of LES quality (Saqr, 2010; Celik et al., 2005). The most established index of LES quality was proposed by Pope (Pope, 2004). Such quality index can be expressed mathematically as a function $M(x, t)$ of space and time (Saqr et al., 2012) as:

$$M(x, t) = \frac{K_{Res}}{K_{Res} + K_{SGS}}$$

where K_{Res} and K_{SGS} are the resolved and subgrid modeled turbulent kinetic energy scalars, respectively. In the present work, K_{Res} can be calculated as: $K_{Res} = \frac{1}{2}(\tilde{u}^2 + \tilde{v}^2)$ and K_{SGS} can be calculated as $K_{SGS} = \frac{\nu_t^2}{(C\Delta)^2}$ where ν_t is the subgrid modeled turbulent kinematic viscosity as calculated in the Smagorinsky model as: $\nu_t = L_s^2 |\bar{S}|$, where L_S is the mixing length for subgrid scales as calculated in Eq. (10) and Δ is the filter length (Eldrainy et al., 2011). Pope (2004) has evidently shown that when $M(x, t) \geq 80\%$ the LES is sufficiently resolved and the flow field is properly resolved. Literature records support Pope's proposition in numerous and variant flows as reported in Mazzei et al. (2016), Fureby (2017), Georgiadis et al. (2010), Eldrainy et al. (2011). In the present work, the quality index $M(x, t)$ was calculated for the computational domain and plotted against LES filter length as in Fig. 9. It is shown that $M(x, t) \geq 80\%$ for filter lengths in the range $\Delta \geq 0.01$. In Fig. 10 a histogram of the filter length shows that approximately 98% of the grid has values of $M(x, t)$ larger than 90% which satisfies Pope's criteria for fully resolved LES.

Since one of the work main objectives is to study the stall regime, therefore, an accurate simulation for the stall must be done. The following Fig. 11 illustrates that a comparison between different models to simulate two dimensional NACA0015 in an unsteady flow with stall angle (13.6°) for NACA0015 with Reynolds number equals to 2×10^5 from experimental data (Torresi et al., 2009, 2007) was presented. The comparison uses only the stall angle to identify which model can present it. The Large Eddy Simulation model (LES) gives good results for the torque coefficient value, while, other models cannot
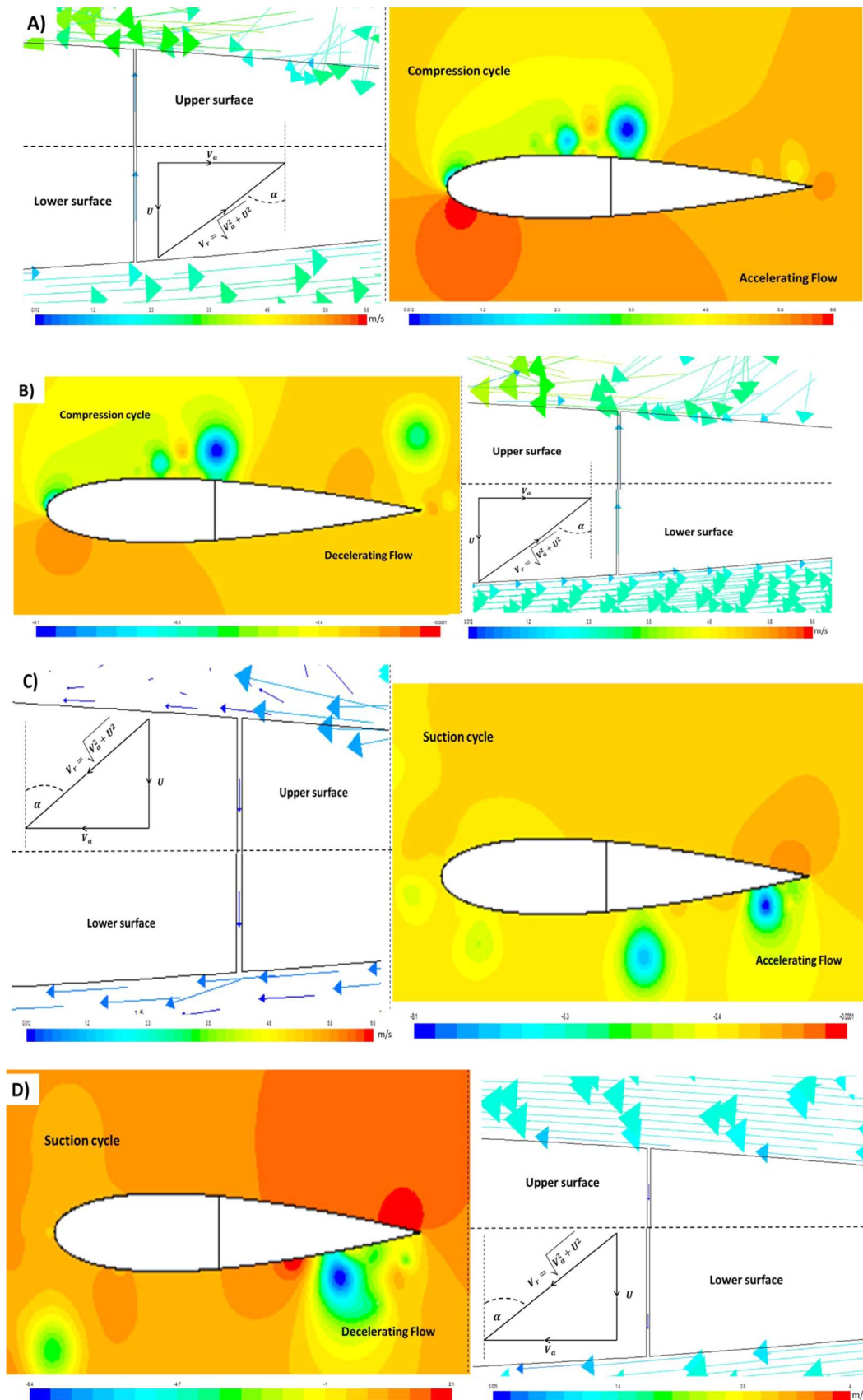
Fig. 17. Factors affecting determination of the slot velocity direction for the pressure distribution and velocity vector direction A) accelerating flow at compression cycle B) decelerating flow at compression cycle C) accelerating flow at suction cycle D) decelerating flow at suction cycle.
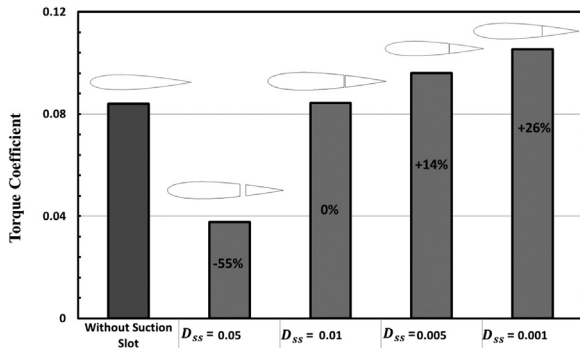
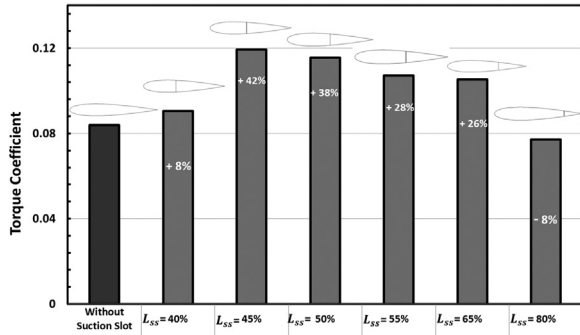**Fig. 18.** Torque coefficient for different D_{ss} at stall angle.

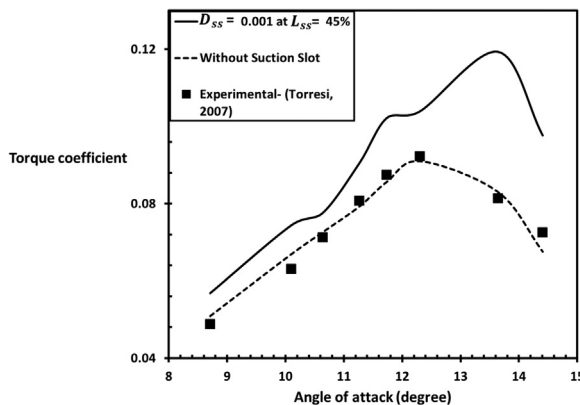**Fig. 19.** Torque coefficient for suction slots at different L_{ss} at 13.64°.

Fig. 20. Suction slot with optimum L_{ss} (45%) and optimum D_{ss} (0.001 m) at different angles of attack.

predict the stall angle. The LES model has shown high disturbance for the path line of the flow stream and the pressure distribution at the upper surface, which leads to the stall condition. The larger turbulent separated zone of the LES may be a reason for the lower value of the lift force (Richez et al., 2007). The LES has shown that some vortexes were formed and caused to appear a fluctuation behavior of pressure distribution on the upper surface of the airfoil, whereas other models

were not able to predict it (Rezaei et al., 2013). On the other hand, the unsteady RANS turbulence modeling has shown a quite dissipative character that attenuates the instabilities and the vortex structures related to the dynamic stall (Martinat et al., 2008). Therefore, the LES model will be used to investigate the stall behavior.

Large Eddy Simulation model was used to model the flow around NACA0015 airfoil in order to give the best agreement with experimental data adopted from Torresi et al. (2009, 2007) and Nomura et al. (2003). The Large Eddy Simulation model gives excellent results when they are used to simulate the airfoil in stall condition, according to literature survey (Dahlstrom, 2003; Richez et al., 2007; Kawai and Asada, 2013; Alferez et al., 2013; Kim et al., 2015; AlMutairi et al., 2015; Armenio et al., 2010; Hitiwadi et al., 2013; Bromby, 2012).

Although LES is a 3D model by definition, there have been numerous successful attempts to use it in 2D applications. For example, flow over obstacles (Skyllingstad and Wijesekera, 2004), hump (Avdis et al., 2009), block (Cheng and Porté-Agel, 2013), airfoils (Hitiwadi et al., 2013; Tenaud and Phuoc, 1997; Shehata et al., 2017a) and Hills (Chaudhari et al., 2014). Other two dimension model applications include the problems dealing with, dam-break (Özgökmen et al., 2007), mechanism of pollutant (Michioka et al., 2010; Chung and Liu, 2013), heat transfer (Andrej Horvata and Marnb, 2001; Matos et al., 1999), turbulent Convection (Chen and Glatzmaier, 2005) and Parallel Blade Vortex (Liu et al., 2012). The flow under investigation occurs due to sinusoidal velocity signal in the XY plane, with no other velocity signals in other domains. Hence, all the main flow phenomena of interest occurs in the XY plane except for the vortex stretching and secondary shedding which occur in the XZ and YZ planes. The authors have reviewed the 2D assumption of the flow under consideration in their recent extensive review paper (Shehata et al., 2017) and concluded that the 2D assumptions are not influential in the flow structure nor the aerodynamic performance of the airfoil under oscillating flow. Hence, the governing equations were reduced to two dimensional form, and solved accordingly. Consequently, and given the fact that this reduction is physically valid, the method of solution of the governing equation (i.e. LES) must follow the coordinate formalism of the governing equations, hence it was solved as two-dimensional problem. In this work two sets of experimental data were used to validate the numerical model from references. First, experimental data from Refs. Torresi et al. (2009, 2007) are used to simulate and validate the stall condition. Details of the first validation case, where Wells turbine prototype are under investigation, is characterized by the following parameters: hub radius, is equal to101 mm; tip radius, equal to 155 mm; NACA0015 blade profile with constant chord length, equal to 74 mm; and number of blades, equal to 7. Therefore, the hub-to-tip ratio, and the solidity, is equal to 0.65 and 0.64, respectively. The uncertainty in the measurements is 5%. The blades have been produced with composite material reinforced by carbon fiber with suited attachment. Second, experimental data from Ref. Nomura et al. (2003) is adopted to simulate and validate the unsteady sinusoidal wave inlet velocity. Details of the second validation case, where experimental data for unsteady forces (F_D) acting on a square cylinder in oscillating flow with nonzero mean velocity are measured. The oscillating air flows are generated by a unique AC servomotor wind tunnel. The generated

Table 4
The improvement percentage between NACA0015 without suction slot and with suction slot at optimum L_{ss} and D_{ss} under unsteady flow with non-oscillating velocity.

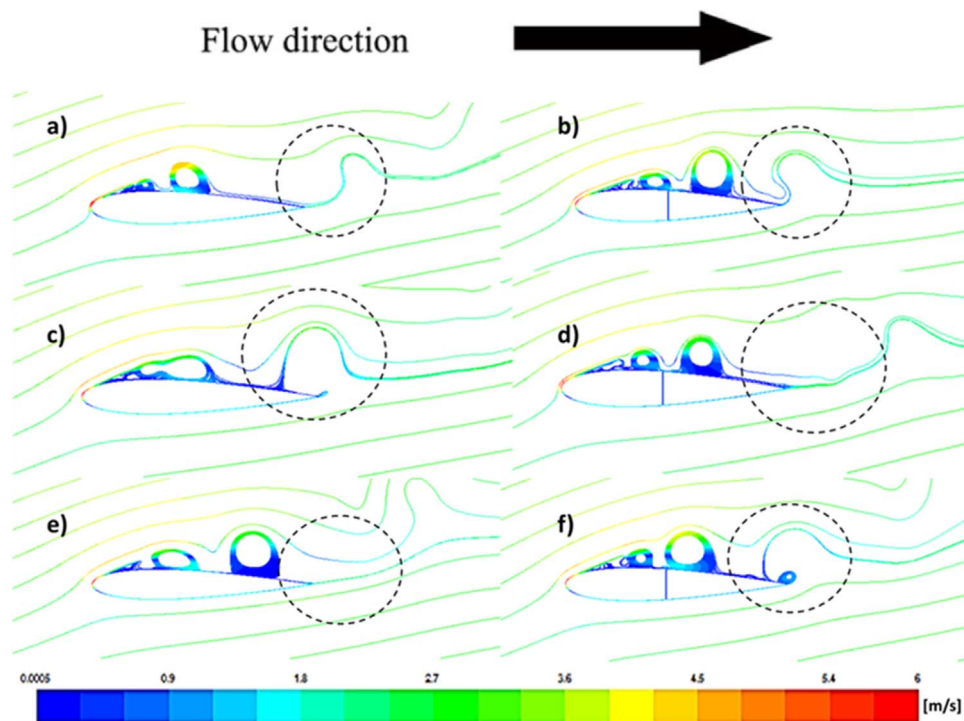| Torque Coefficient	Angle of attack (Degree)							
	8.709	10.097	10.639	11.266	11.734	12.304	13.642	14.406
Without Suction Slot	0.0509	0.0669	0.0726	0.0793	0.0856	0.091	0.083	0.0676
D_{ss}=0. 001 **m at** L_{ss}=45%	0.0568	0.0744	0.0776	0.091	0.1022	0.104	0.119	0.0977
Improvement %	12	11	7	14	19	14	44	45

Fig. 21. The path-line for mean velocity magnitude at certain velocity equal to 2.92 m/s unsteady input flow with non-oscillating velocity, a) and b) 12.3°, c) and d) 13.6°, e) and f) 14.4°. (For interpretation of the references to color in this figure, the reader is referred to the web version of this article.)
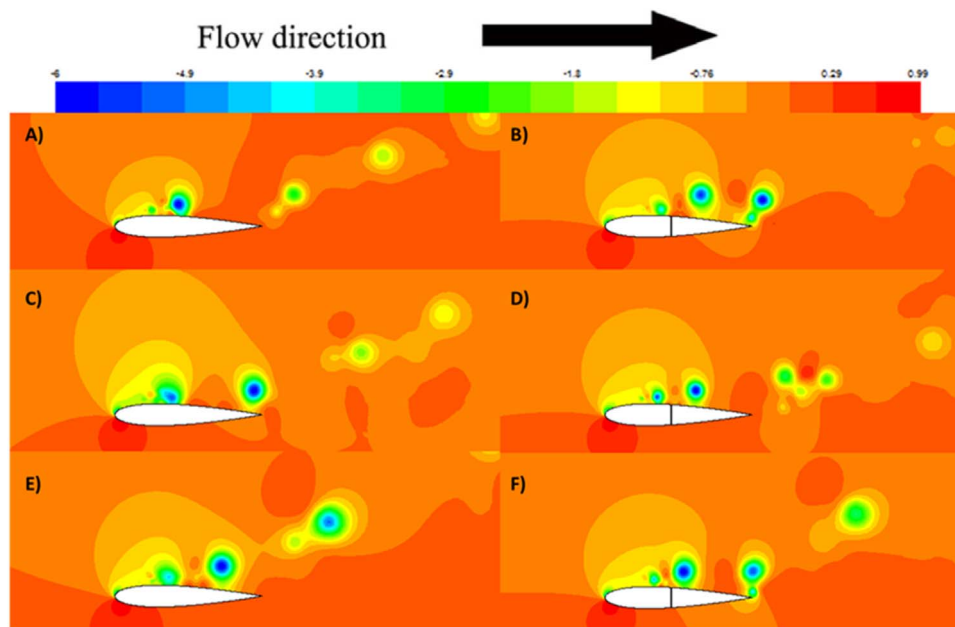

Fig. 22. The pressure coefficient around the airfoil, unsteady input flow with non-oscillating velocity, A) and B) 12.3°, C) and D) 13.6°, E) and F) 14.4°.

velocity histories are almost exact sinusoidal waves.

For unsteady flow with non-oscillating velocity, Fig. 12 shows a very good agreement between the measured torque coefficient from Refs. Torresi et al. (2009, 2007) and the calculated torque coefficient from CFD result at Reynolds number of 200000. It can be noted that the computational model has approximately the same stall condition value as the reference. The comparison between those results and the percentage of error are listed in Table 1. Furthermore, for an unsteady flow with sinusoidal inlet velocity, Figs. 13 and 14 show a good agreement between measured drag force from Ref. Nomura et al.

(2003) and predicted drag force from CFD at two different frequencies (2 Hz and 1 Hz). It can be shown from Figs. 13 and 14 that the computational model has almost the same behavior of oscillating flow condition as the reference; see also the error percentage in Table 2 for the two frequencies. Finally, Fig. 15 displays the results of computational model under sinusoidal inlet flow velocity with experimental data from Torresi et al. (2009, 2007) and an excellent agreement is achieved. The comparison of these results and the percentage of error are summarized in Table 3. The Large Eddy Simulation computational model has approximately the same stall condition value as the
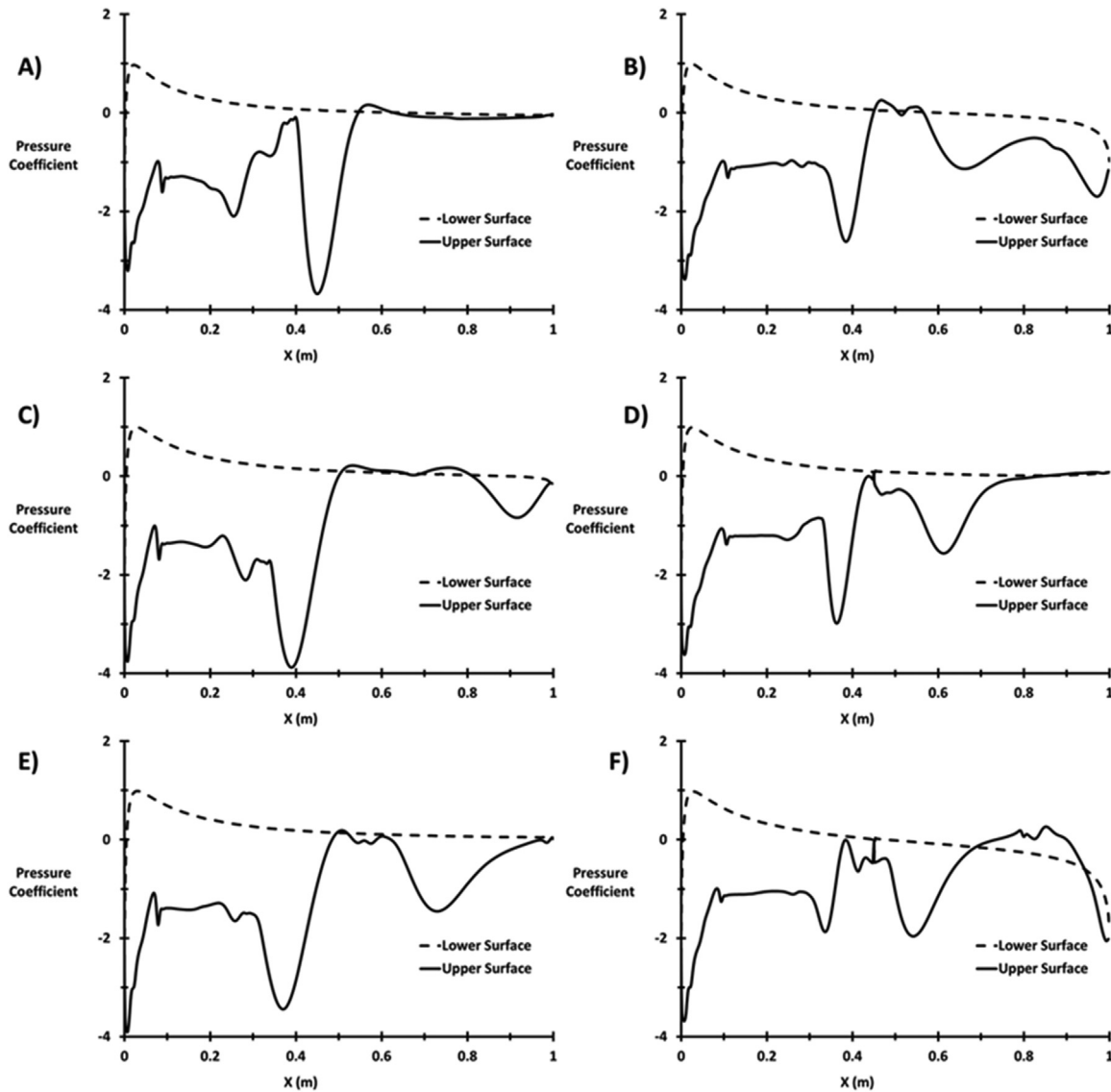
Fig. 23. Pressure coefficient distribution on the upper and lower surface of the airfoil, A) and B) 12.3°, C) and D) 13.6°, E) and F) 14.4°.
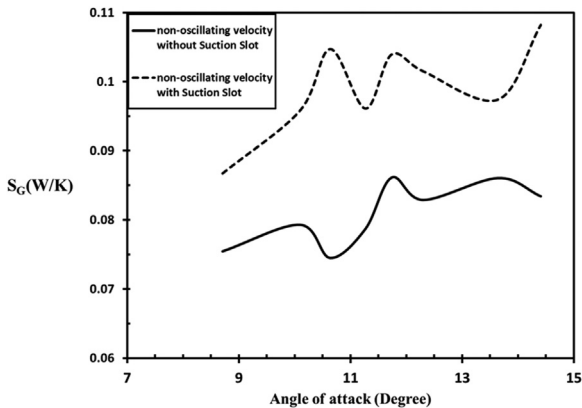

Fig. 24. The effect of suction slot on the global entropy generation rate with different angle of attack.

reference.

4. Results and discussion

A slot with certain diameter at various locations from the leading

edge was created with a shape of NACA0015 from Refs. Torresi et al. (2009, 2007), see Fig. 16. The diameter and location for the slot were changed in order to obtain an optimum value. During the compression cycle, this slot suctions the flow from lower surface (high pressure) and blows it to the upper surface (low pressure), see Fig. 17. Where, Fig. 17A is for the accelerating flow at 1.3 s and B is for the decelerating flow at 1.65 s with Reynolds number equal to 190000. Furthermore, this pressure difference affecting on the velocity vector direction, as it can be noted in Fig. 17 for the velocity vector of the velocity magnitude. On the other hand, during the suction cycle in Fig. 17C (4.35 s) and D (4.6 s), the slot suctions the flow from the upper surface (high pressure) and blows it to the lower surface (low pressure) in both the accelerating and decelerating flow at Reynolds number equal to 190000. It can be also noted that the pressure difference affecting on the velocity vector direction, which it refer to the flow direction. Therefore, it can be concluded that the factor affecting determination of the slot velocity direction is the pressure difference. The slot will be defined as a suction slot in the analysis and results which were presented henceforth. The test cases investigated are under 1) unsteady flow with non-oscillating velocity and 2) sinusoidal wave condition.
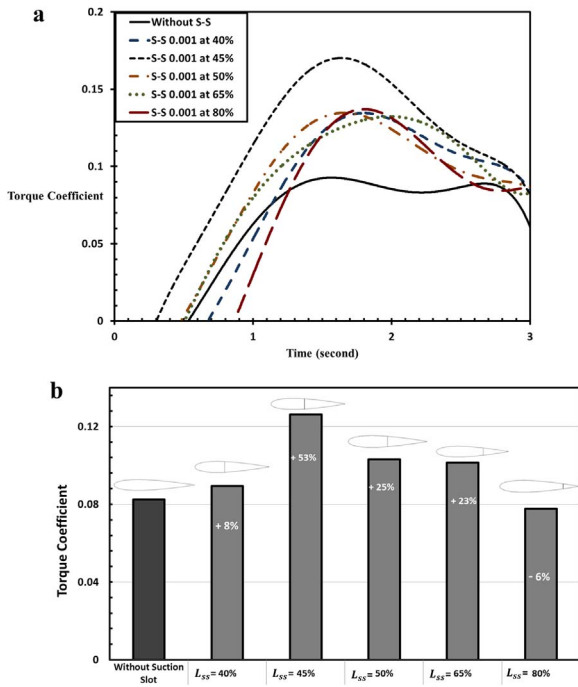
Fig. 25. a) Suction slot with D_{ss} equal to 0.001 m at different L_{ss} for instantaneous torque coefficient at 13.6° under unsteady flow with sinusoidal inlet velocity b) suction slot with D_{ss} equal to 0.001 m at different L_{ss} for average torque coefficient at 13.6° under unsteady flow with sinusoidal inlet velocity.
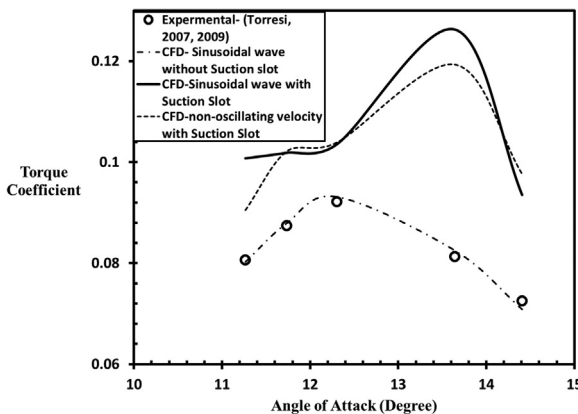

Fig. 26. Suction slot with optimum L_{ss} (45%) and optimum D_{ss} (0.001 m) at different angles of attack under unsteady flow with sinusoidal inlet velocity.

Table 5
The improvement percentage between NACA0015 without suction slot and with suction slot at optimum L_{ss} and D_{ss} under unsteady flow with sinusoidal inlet velocity.

Torque Coefficient	Angle of attack (Degree)				
	11.266	11.734	12.304	13.642	14.406
Without Suction Slot	0.0803	0.0879	0.0931	0.0825	0.0709
D_{ss}=0. 001 **m at** L_{ss}=45%	0.1008	0.1019	0.104	0.126	0.094
Improvement %	26	16	11	53	32

4.1. Unsteady flow with non-oscillating velocity

The effect of suction slots in the airfoils behavior will be shown in the following three sections.

4.1.1. Torque coefficient and Stall angle

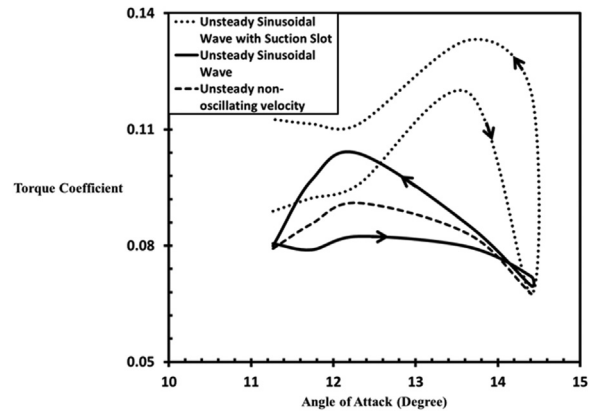Fig. 18 demonstrates the effect of varying D_{ss} on the torque

Fig. 27. The hysteretic behavior due to unsteady flow with sinusoidal inlet velocity at different angles of attack with optimum L_{ss} (45%) and optimum D_{ss} (0.001 m).

coefficient at the stall angle (13.6°) from Fig. 11 for Refs. Torresi et al. (2009, 2007). All suction slots have L_{ss} up to 65%. It can be remarked that the suction slot with D_{ss} of 0.001 m gives a higher torque coefficient than others. The torque coefficient increases about 26% than the airfoil without suction slot.

Fig. 19 exemplifies the effect of L_{ss} on the torque coefficient at the stall angle (13.6°) with D_{ss} equal to 0.001 m. It can be discerned that, the L_{ss} equal to 45%, gives a higher torque coefficient than other L_{ss}. Where, the torque coefficient increases about 42% than the airfoil without suction slot.

Fig. 20 reveals the effect of suction slot with optimum L_{ss} and optimum D_{ss} on the torque coefficient at different angles. It is clearly noted that the improvement of torque coefficient at different angles (from 7% to 19%), especially at stall regime (from 44% to 45%), which is caused by the delay in stall angle. For more details about the value of improvement in torque coefficient, see Table 4.

4.1.2. Flow field around the airfoil section

Fig. 21 shows path lines colored by mean velocity magnitude at maximum value of torque coefficient and stall condition. In addition, it also shows the effect of suction slot on the boundary layer and flow field around the airfoil. Also, it highlights the amount of the difference between the effects of suction slot before and after the stall condition. This difference is clearly indicated between Fig. 21a, b for 12.3° and c, d for 13.6°. The effect of suction slot on the separation layer at the end of blade in Fig. 21a, b was small. This is due to the fact that the tow Figure did not have the stall condition yet. On the other hand, the effect of suction slot on the separation layer in Fig. 21c and d is significant because Fig. 21c represents the data in the stall condition however, Fig. 21d does not. As for Figures e and f, the two airfoils are in stall regime. Figs. 22 and 23 clarify the pressure distribution around the upper and lower surface of airfoil at maximum velocity (2.92 m/s) with different angles of attack. It can be shown that the low pressure area at the trailing edge was increased with the increase in angle of attack for the airfoil without slots. From Fig. 23A), C) and E) it can be noted that the low pressure zones and disturbances at the trailing edge for the upper surface was created the layer separation at the trailing edge and it was also increased by the increase in angle of attack. The effect of the suction slot was very clear at the pressure distribution around the airfoil, where it was more significant after the stall angles (13.6 and 14.4°) than that before the stall (12.3°). The difference between the pressure value for the upper and lower surface at the trailing edge was decreased by adding suction slot to the airfoil especially at the stall angles.
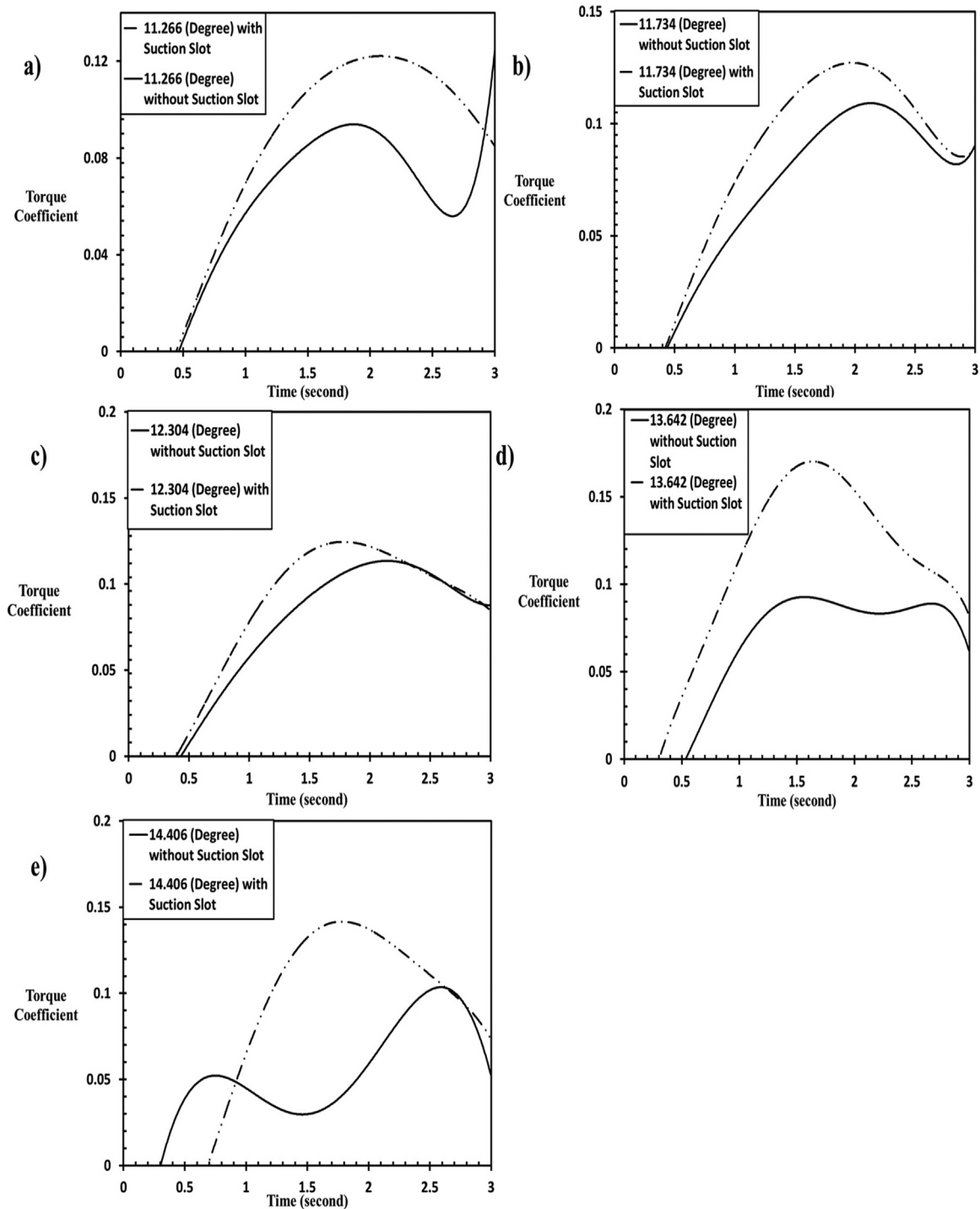
Fig. 28. Torque coefficients at compression cycle for different angles of attack under unsteady flow with sinusoidal inlet velocity with optimum L_{ss} (45%) and optimum D_{ss} (0.001 m), a) 11.3°, b) 11.7°, c) 12.3°, d) 13.6°, e) 14.4°.

4.1.3. Second law analysis

Fig. 24 shows that the suction slot has a negative effect on the second law efficiency, where the global entropy generation rate increases at all angles from (14–41%). The 10.6° angle of attack (before the stall) has the highest difference in global entropy generation rate by 41% due to suction slot. On the other hand, 8.7 (before the stall) and 13.6 (after the stall) degree angle of attack have the lowest difference in global entropy generation rate by 14% due to suction slot. Otherwise, the 10.1, 11.27, 11.74 and 12.3 (before the stall) degree have the same difference in global entropy generation rate by

21.5% due to suction slot. Also, the 14.4 (after the stall) degree has a difference in the global entropy generation rate by 30%. This phenomenon suggests that the change in velocity gradient due to the suction slot has a direct impact on the entropy generation.

4.2. Sinusoidal wave

4.2.1. Torque coefficient and Stall angle

Fig. 25a) clarifies the instantaneous torque coefficient at compression cycle for different L_{ss}, while Fig. 25b) shows the average value of
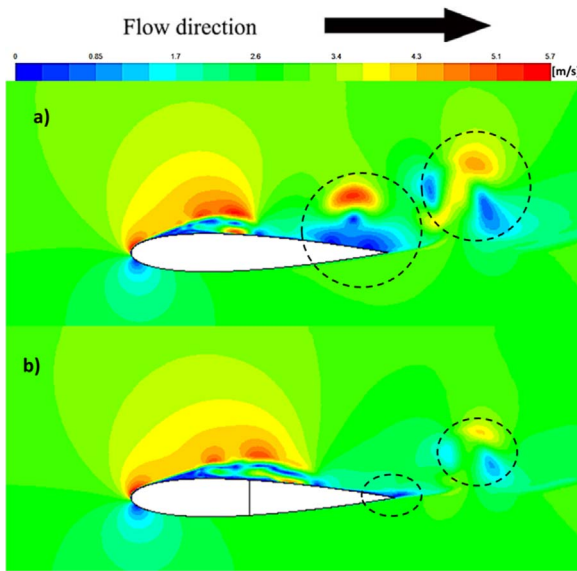
Fig. 29. Velocity magnitude contours at maximum velocity equal to 2.92 (m/s) for sinusoidal input flow, at 12.3°, before the stall.

Fig. 31. Path-line colored by mean velocity magnitude at maximum velocity equal to 2.92 (m/s) for sinusoidal input flow, at 12.3°, before the stall. (For interpretation of the references to color in this figure legend, the reader is referred to the web version of this article.)

torque coefficient. These values are at citrine angle of attack of 13.6° and citrine D_{ss} equal to 0.001 m. The L_{ss} equal to 45%, gives a higher torque coefficient value than other L_{ss}. This result is consistent with the result from previous section. Fig. 26 shows the effect of L_{ss} with 45% and D_{ss} equal to 0.001 m, on torque coefficient at different angles. The improvement of torque coefficient is clearly noted before the stall regime (from 11% to 26%) and at stall regime (from 32% to 53%). Table 5 shows more details about the value of improvement in torque coefficient.

Fig. 27 explains the hysteretic behavior due to the reciprocating flow, the performance of the Wells turbine has a hysteretic loop in which the values of torque coefficient in the accelerating flow is smaller
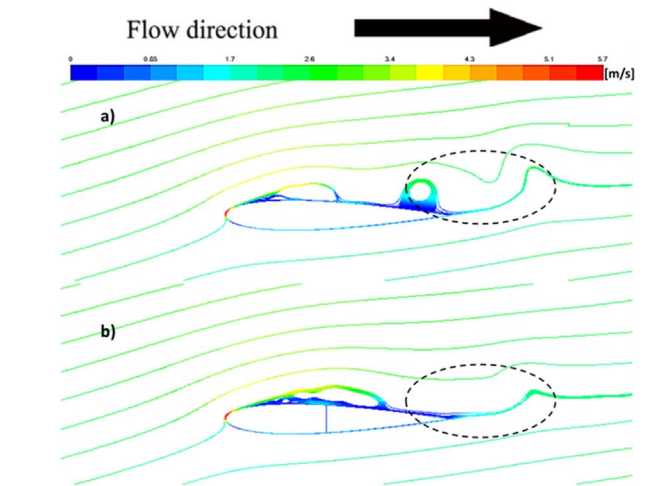
than in the decelerating flow. The hysteretic behavior was studied experimentally and numerically in the Refs. Setoguchi et al. (2003a, 2003b, 1998), Mamun (2006), Mamun et al. (2004), Kinoue et al. (2003a, 2004, 2003b), Kim et al. (2002), Thakker and Abdulhadi (2008, 2007). By a numerical simulation using a quasi-steady analysis, it can be that the only study which simulated the hysteretic behavior after the stall is Setoguchi et al., (2003a). Moreover, Fig. 27 highlights the hysteretic behavior after adding the suction slot to the airfoil which has the same behavior. Furthermore, it delays the stall regime in addition the torque coefficient. The torque coefficients at compression cycle for different angles of attack are shown in Fig. 28. It can be observed that for all angles, the suction slot increases the torque coefficient. Fig. 28d) and e) have the highest increase value in
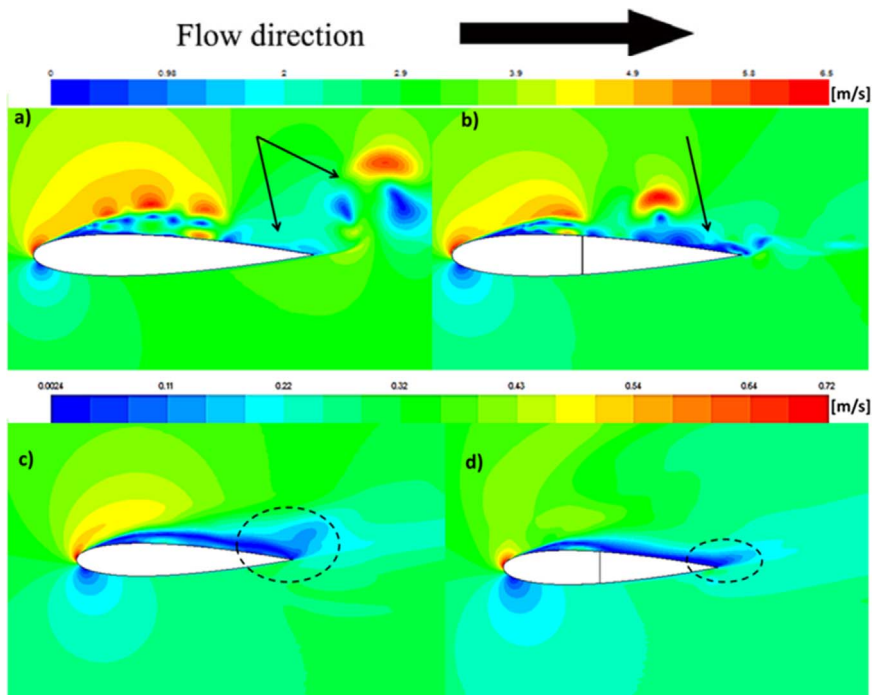

Fig. 30. a) and b) Velocity magnitude contours, c) and d) mean velocity magnitude contours, at maximum velocity equal to 2.92 (m/s) for sinusoidal input flow, at 13.6°, after the stall.
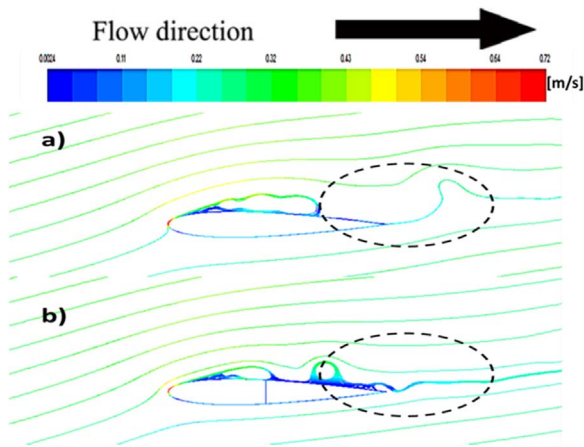
Fig. 32. Path-line colored by mean velocity magnitude at maximum velocity equal to 2.92 (m/s) for sinusoidal input flow, at 13.6°, after the stall. (For interpretation of the references to color in this figure legend, the reader is referred to the web version of this article.)

comparison to other Figures. Whereas, the torque coefficient was increased by (approximately) 26% in Fig. 28a), 16% in Fig. 28b) and 11% in Fig. 28c). The stall regime was delayed in Fig. 28d), in addition, the torque coefficient was increased by (approximately) 53% and by (approximately) 32% in Fig. 28e). Furthermore, the behavior of torque coefficient with the suction slot curve was more stable than that without suction slot which is increased from the amount of highest value, as it see in Fig. 28d) and e).

4.2.2. Flow field around the airfoil section

The flow structures over the NACA0015 airfoil in oscillating flow was shown in Figs. 29 and 30. Fig. 29 accentuates the contour of velocity magnitude at maximum velocity and angle of attack equal to 12.3° (before the stall). The improvement effect of the suction slot on flow structures is clear when compared between Fig. 29a) and b), especially in, the separated layer regime at the end of airfoil. The same behavior occurs in Fig. 30a) and b) for the contour of velocity magnitude, and also in c) and d) for mean velocity magnitude from unsteady statistics. Fig. 30 emphasize the improvement effect of the suction slot on flow structures at maximum velocity and angle of attack equal to 13.6° (after the stall). The suction slot has a direct effect on the flow structures at the end of blade, which leads to an improvement in the separation regime.

The path-lien colored by means of velocity magnitude highlight the improvement effect of the suction slot on the separation layers in Figs. 31 and 32. It can be noted that by adding the suction slot in the airfoil, this suction slot was decreased from the separation layer at the end of airfoil. By comparing Fig. 31 (before the stall) and Fig. 32 (after the stall), it can be also noted that, the improvement effect of suction slot on separation layers was increased in the stall regime. The pressure distribution around the upper and lower surface at 12.3° before the stall (Fig. 33) and 13.6° after the stall (Fig. 34) were presented. The effect of the suction slot on the trailing edge area was appearing through the decrease from the low pressure area that cause disturbances in the path line at the trailing edge area and it extends to the area beyond the trailing edge. The pressure distribution after suction slot location (L_{SS}=45%) at the upper surface has a direct effect in its value before and after the stall. The difference in pressure value between the upper and lower surface after the slot location (Fig. 34) was decreased due to the slot effect. This decrease made the pressure distribution behavior similar to the pressure distribution for the upper surface of the airfoil before the stall (Fig. 33) which led to a delay on the stall condition.

4.2.3. Second law analysis

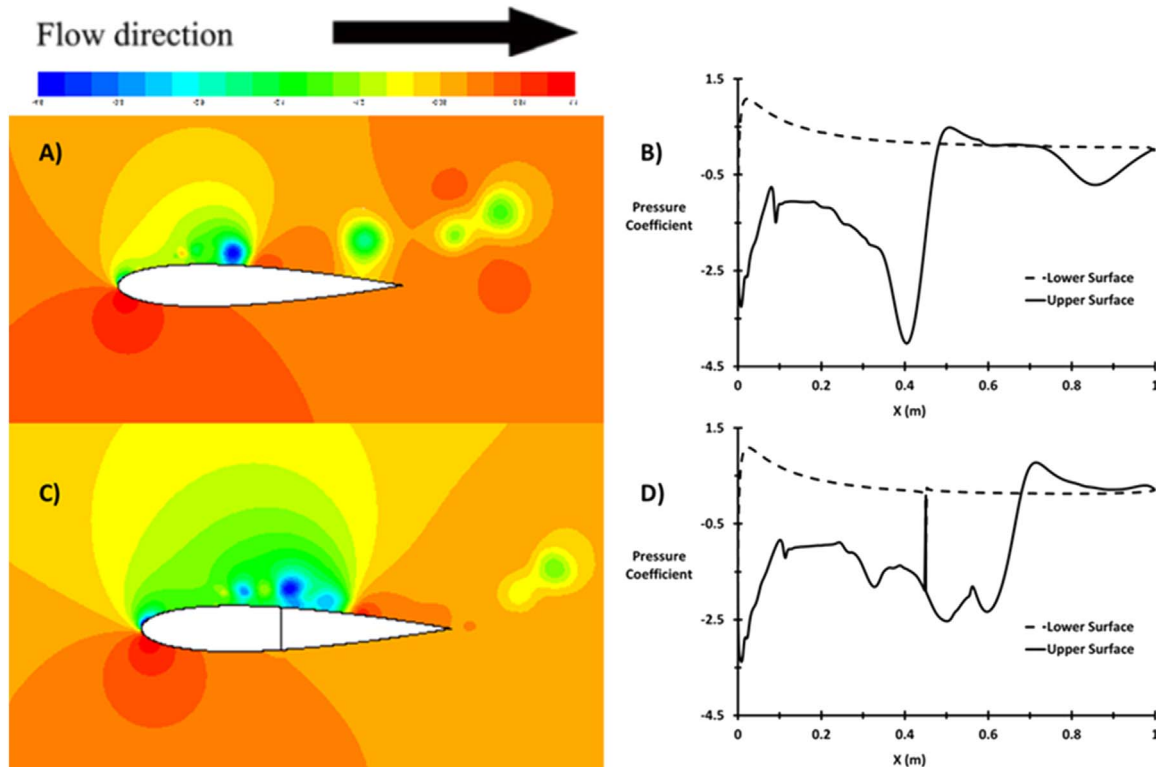The numerical simulations are used to obtain local entropy viscosity

Fig. 33. The pressure distribution at maximum velocity equal to 2.92 (m/s) for sinusoidal input flow, at 12.3°, before the stall.
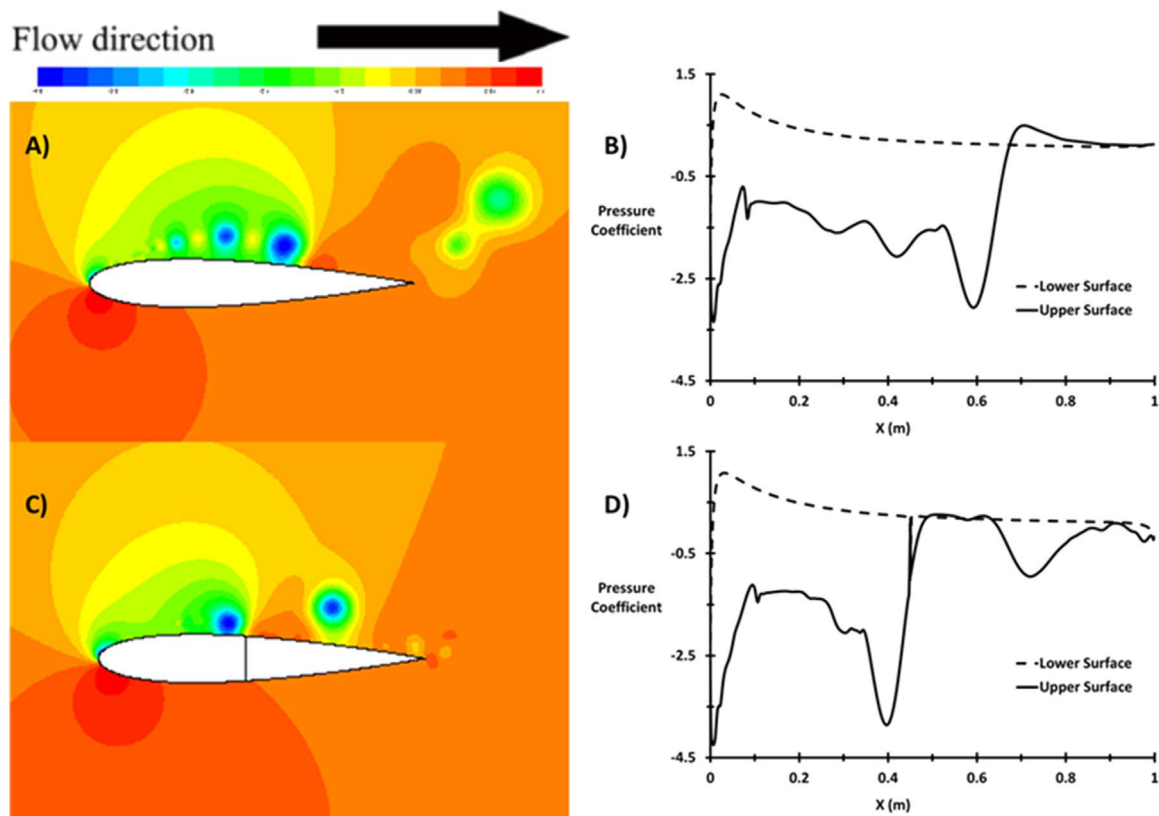
Fig. 34. The pressure distribution at maximum velocity equal to 2.92 (m/s) for sinusoidal input flow, at 13.6°, after the stall.

predictions of the different angle of attack. Figs. 35 and 36 highlight the suction slot effect in the entropy behavior when a flow is accelerating and decelerating in compression cycle. Consequently, the entropy generations rate varies with the Reynolds number. The change of Reynolds number values results as a consequence to using sinusoidal wave boundary conditions. Suction slot have negative effect on the entropy behavior in both accelerating and decelerating flow. Otherwise, at some Reynolds numbers, the suction slot decreased from the entropy generation. As an illustration, Fig. 35e) at Reynolds number is less than 100000 in accelerating flow. Also, Fig. 36a) at Reynolds number is equal to 160000 in decelerating flow. The airfoil with the suction slot at 11.3° has an average increase in the entropy generation rate by 22% than that without the suction slot for the accelerating flow. Whereas, on the one hand, the maximum difference in the entropy generation rate was found at Reynolds number to be equal to 193000 and 200000 by 36% than that without the suction slot. On the other hand, the minimum difference in the entropy generation rate was found at Reynolds number from 50000 to 100000 by 11% than that without the suction slot; see Fig. 35a). For decelerating flow at 11.3°, it can be noted that the maximum increase in the entropy generation rate due to the suction slot was 35% at Reynolds number equal to 55000. Additionally, on one hand, the entropy generation rate was decreased than that without the suction slot by −23% at 160000 Reynolds number. This increase and decrease in the entropy generation rate for the airfoil with the suction slot gives an average value equal to 0% at decelerating flow, see Fig. 36a). From Fig. 35b), it can be noted that the maximum increase in the entropy generation rate is 39% due to the suction slot for accelerating flow at 198000 Reynolds number. On the other hand, the minimum increase in the entropy generation rate is 11% at Reynolds number from 78000 to 100000, with an average

percentage 22% for the 11.7°. For decelerating flow at 11.7°, the maximum increase in the entropy generation rate is 31% at 30000 Reynolds number and the minimum value is −14% at 175000 Reynolds number, due to the decrease of the entropy generation rate than that without the suction slot. This increase and decrease in the entropy generation rate for the airfoil with the suction slot gives an average value equal to 14% at decelerating flow, see Fig. 36b). The 12.3° at accelerating flow gives maximum increase by 35% at 200000 Reynolds number and minimum increase by 6% Reynolds number from 78000 to 100000 with an average percentage 21%, see Fig. 35c). Otherwise, Fig. 36c) shows the maximum increase by 34% at 80000 Reynolds number and minimum increase by 3% 160000 Reynolds number with an average percentage 18%.

The airfoil with the suction slot at 13.6° has an average increase in the entropy generation rate by 51% than that without the suction slot for the accelerating flow. Whereas, the maximum different in the entropy generation rate was found at Reynolds number to be equal to 28400 by 152% than that without suction slot. On the other hand, the minimum difference in the entropy generation rate was found at 160000 Reynolds number by 17% than that without the suction slot, see Fig. 35d). For decelerating flow at 13.6°, the maximum increase in the entropy generation rate is 36% at 160000 Reynolds number and the minimum value is −5% at 80000 Reynolds number, due to the decrease of the entropy generation rate than that without the suction slot. This increase and decrease in the entropy generation rate for the airfoil with the suction slot gives an average value equal to 19% at decelerating flow, see Fig. 36d). The 14.4° at accelerating flow gives maximum increase by 26% at 185000 and 198000 Reynolds number, and minimum increase by −30% Reynolds number from 54000 to 80000 due to the decrease of the entropy generation rate than that without
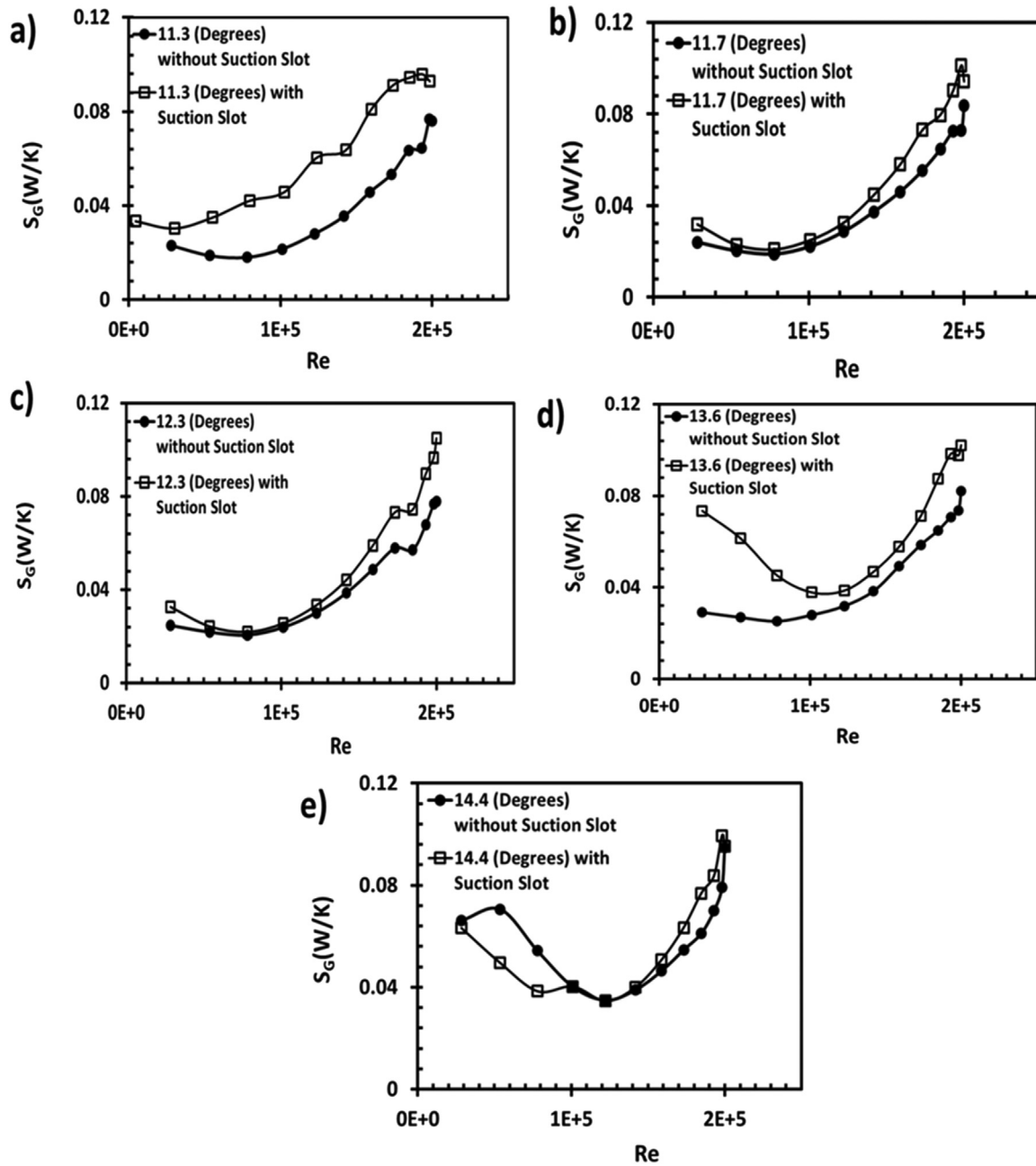
Fig. 35. The global entropy generation rate variation with different Reynolds number at accelerating flow in compression cycle for different angles of attack with optimum L_{ss} (45%) and optimum D_{ss} (0.001 m).

suction slot. This increase and decrease in the entropy generation rate for the airfoil with the suction slot gives an average value equal to 3% at accelerating flow, see Fig. 35e). Otherwise, Fig. 36e) shows the maximum increase by 46% at 80000 and 143000 Reynolds number, and minimum increase by 0% 100000 Reynolds number with an average percentage 21%.

Furthermore, as an average value for the compression cycle, the suction slot was increased from the global entropy generation rate, see Fig. 37. This led to a decrease in the second law efficiency, see Fig. 38. From Figs. 37 and 38, it is deducted that the minimum value for the global entropy generation rate and maximum second law efficiency occurs at 11.7° for airfoil without the suction slot. On the other hand, the minimum value for the global entropy generation rate and maximum second law efficiency occurs at 11.3° for airfoil with the suction slot.

5. Conclusions

A two-dimensional incompressible unsteady flow is simulated for airfoil under different conditions to investigate the effect of airfoil with a suction slot on the torque coefficient and a stall condition as well as the entropy generation due to viscous dissipation. The modeling results show that D_{ss} and L_{ss} have different effects on the torque coefficient and stall condition. Therefore, not all the parameters tested in the present study achieve a positive effect in terms of improved blade torque. In general, it can be concluded that the decrease in D_{ss} comes with an increase in torque coefficient. The smallest tested D_{ss} is 0.001 m, since any smaller value would not be practical in real industries. Also, the best L_{ss} is locating (approximately) at 45% from the leading edge (at 13.6°). By applying these conditions we can achieve a 53% increase in the torque coefficient at stall regime (13.6°). The increase in torque
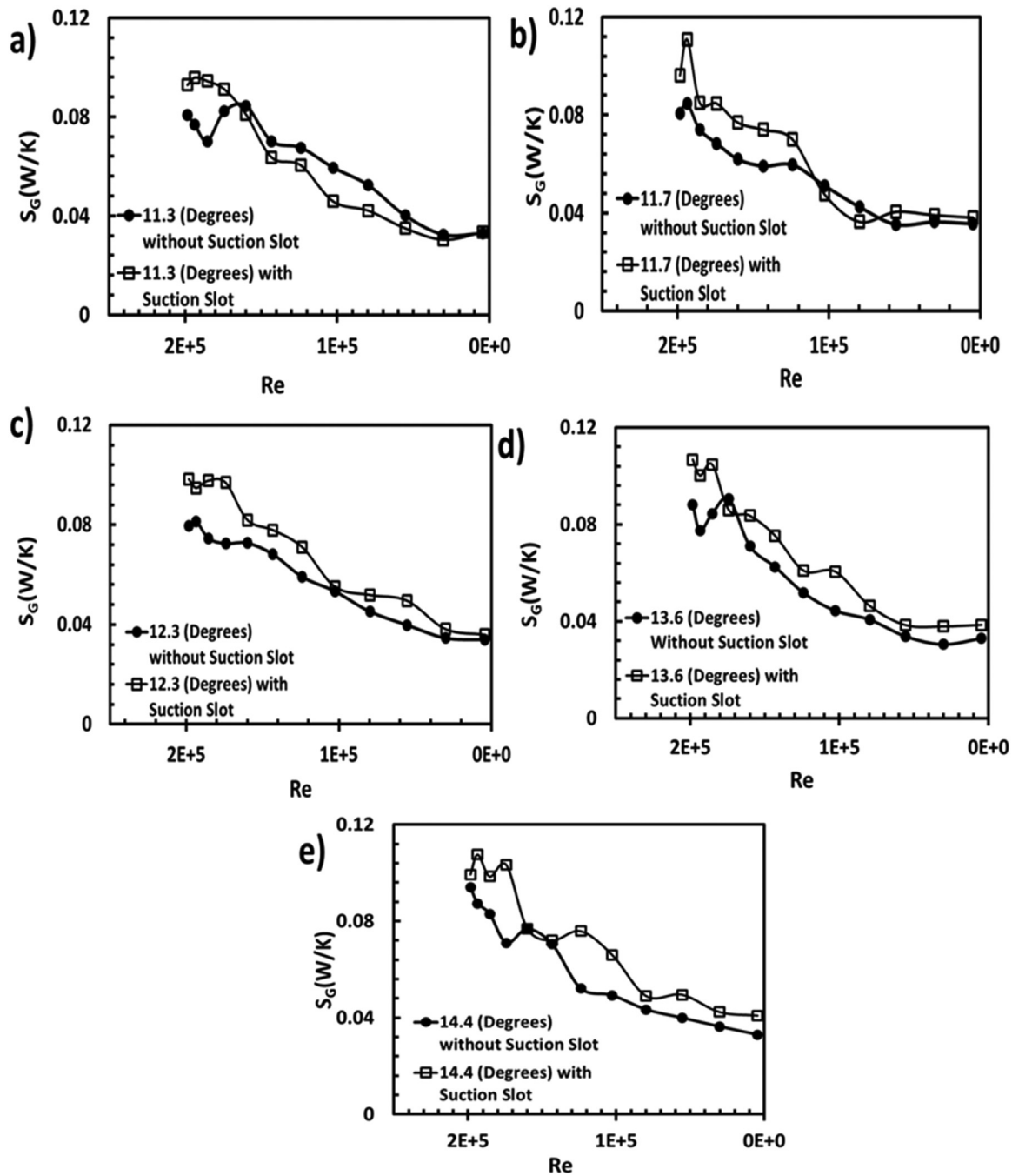
Fig. 36. The global entropy generation rate variation with different Reynolds number at decelerating flow in compression cycle for different angles of attack with optimum L_{ss} (45%) and optimum D_{ss} (0.001 m).

coefficient, due to the suction slot, ranges from 11% to 26% before the stall regime. Hence, the regime after the stall increases in torque coefficient varying from 32% to 53%. The main reason behind this observation is due to the delay of the stall condition. The suction slot increases the torque coefficient and delays the stall angle which further leads to an increase of first law efficiency. On the other hand, it decreases the second law efficiency. Thus, if the turbine operates under high flow coefficient (angle of attack), it is strongly suggested to use the

suction slot to improve the performance at the stall condition. Otherwise, it may not be effective. Future research should focus on improving the first law efficiency with a minimize entropy generation, by using numerical algorism and experimental test, in order to enhance the overall Wells turbine performance under flow control method. Furthermore, it should investigate the suction slot and its location in the third direction (Z axis) via three-dimensional simulation.
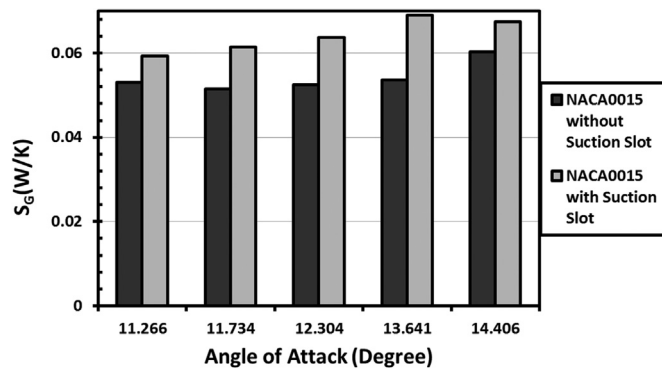
Fig. 37. The global entropy generation rate in compression cycle for different angles of attack with optimum L_{ss} (45%) and optimum D_{ss} (0.001 m).
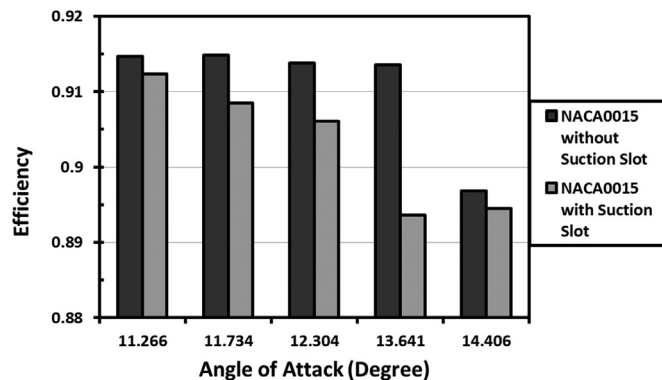

Fig. 38. The second law efficiency in compression cycle for different angles of attack with optimum L_{ss} (45%) and optimum D_{ss} (0.001 m).

Acknowledgements

References

Akcayoz, E., Tuncer, I.H., 2009. Numerical Investigation of Flow Control Over an Airfoil Using Synthetic Jets and its Optimization. International Aerospace Conference, Turkey.

Alferez, N., Mary, I., Lamballais, E., 2013. Study of stall development around an airfoil by means of high fidelity large Eddy simulation. Flow Turbul. Combust. 91 (3), 623–641.

AlMutairi, J., AlQadi, I., ElJack, E., 2015. Large Eddy Simulation of a NACA-0012 Airfoil Near Stall. 20, pp. 389–395.

Andrej Horvata, I.K., Marnb, Jure, 2001. Two dimensional large eddy simulation of turbulent natural convection due to internal heat generation. Int. J. Heat Mass Transf. 44 (21), 3985–3995.

Armenio, V., Geurts, B., Fröhlich, J., 2010. Large Eddy Simulation of Flow Around an Airfoil Near Stall. 13, pp. 541–545.

Avdis, A., Lardeau, S., Leschziner, M., 2009. Large eddy simulation of separated flow over a two-dimensional hump with and without control by means of a synthetic slot-jet. Flow Turbul. Combust. 83 (3), 343–370.

Baskut, O., Ozgener, O., Ozgener, L., 2010. Effects of meteorological variables on exergetic efficiency of wind turbine power plants. Renew. Sustain. Energy Rev. 14 (9), 3237–3241.

Baskut, O., Ozgener, O., Ozgener, L., 2011. Second law analysis of wind turbine power plants: Cesme, Izmir example. Energy 36 (5), 2535–2542.

Bejan, A., 1995. Entropy Generation Minimization: The Method of Thermodynamic Optimization of Finite-Size Systems and Finite-Time Processes. Taylor & Francis.

Bejan, A., 1996. Entropy generation minimization – the new thermodynamics of finite-size devices and finite-time processes. Appl. Phys. Rev. 79 (3), 1191–1218.

Boccotti, P., 2007a. Comparison between a U-OWC and a conventional OWC. Ocean Eng. 34, 799–805.

Boccotti, P., 2007b. Caisson breakwaters embodying an OWC with a small opening—part I: theory. Ocean Eng. 34 (5–6), 806–819.

Braslow, A.L., 1999. A history of suction type laminar flow control with emphasis on flight research, NASA History Division. Monogr. Aerosp. Hist., 13.

Brito-Melo, A., Gato, L.M.C., Sarmento, A.J.N.A., 2002. Analysis of Wells turbine design parameters by numerical simulation of the OWC performance. Ocean Eng. 29, 1463–1477.

Bromby, D.Y.A.W., 2012. Large-eddy simulation of unsteady separation over a pitching airfoil at high Reynolds number. In: Proceedings of the Seventh International Conference on Computational Fluid Dynamics (ICCFD7). Big Island, Hawaii.

Celik, I., Cehreli, Z., Yavuz, I., 2005. Index of resolution quality for large eddy simulations. J. Fluids Eng. 127 (5), 949–958.

Chapin, V.G., Benard, E., 2015. Active control of a stalled airfoil through steady or unsteady actuation jets. J. Fluids Eng. 137 (9), 091103.

Chaudhari, Ashvinkumar, et al., 2014. Large Eddy simulation of boundary-layer flows over two-dimensional hills. In: Industrial Mathematics at ECMI 2012, 2012. Springer International Publishing, Switzerland, p. 211–218.

Chawla, J.S., et al., 2014. Efficiency improvement study for small wind turbines through flow control. Sustain. Energy Technol. Assess. 7, 195–208.

Chen, Q., Glatzmaier, G.A., 2005. Large eddy simulations of two-dimensional turbulent convection in a density-stratified fluid. Geophys. Astrophys. Fluid Dyn. 99 (5), 355–375.

Cheng, W.-C., Porté-Agel, F., 2013. Evaluation of subgrid-scale models in large-eddy simulation of flow past a two-dimensional block. Int. J. Heat Fluid Flow 44, 301–311.

Chung, T.N.H., Liu, C.-H., 2013. On the mechanism of air pollutant removal in two-dimensional idealized street Canyons: a large-Eddy simulation approach. Bound.-Layer Meteorol. 148 (1), 241–253.

Collis, S., et al., 2004. Issues in active flow control: theory, control, simulation and experiment. Prog. Aerosp. Sci. 40 (4–5), 237–289.

Curran, R., et al., 1998. Performance prediction of contrarotating wells turbines for wave energy converter design. J. Energy Eng. 124 (2), 35–53.

Curran, R., Folley, M., 2008. Air turbine design for OWCs. In: Cruz, iJ. (Ed.), Ocean Wave Energy. Springer, Berlin, 189–219.

Dahlstrom, S., 2003. Large Eddy simulation of the flow around a high-lift airfoil. In: Department of Thermo and Fluid Dynamics. Chalmers University of Technology, Goteborg, Sweden, p. 62.

DE Moura, C.A.K., Carlos, S., 2013. The Courant–Friedrichs–Lewy (CFL) Condition: 80 Years After Its Discovery 1 ed.. Birkhäuser Basel, Boston.

Dixon, S.L., 1998. Fluid Mechanics, Thermodynamics of Turbomachinery. Pergamon Press Ltd., England.

DK, L., 1992. A proposed modification of the Germano subgrid-scale closure method. Phys. Fluids A 4 (3), 633–635.

Eldrainy, Y.A., et al., 2011. Large eddy simulation and preliminary modeling of the flow downstream a variable geometry swirler for gas turbine combustors. Int. Commun. Heat Mass Transf. 38 (8), 1104–1109.

Falcao, A.Fd., 2004. Stochastic modelling in wave power-equipment optimisation: maximum energy production versus maximum profit. Ocean Eng. 31 (2004), 1407–1421.

Falcao, A.F.d.O., Justino, P.A.P., 1999. OWC wave energy devices with air flow control. Ocean Eng. 26, 1275–1295.

Fernandez, E., Kumar, R., Alvi, F., 2013. Separation control on a low-pressure turbine blade using microjets. J. Propuls. Power 29 (4), 867–881.

Folley, M., Curran, R., Whittaker, T., 2006. Comparison of LIMPET contra-rotating wells turbine with theoretical and model test predictions. Ocean Eng. 33 (8–9), 1056–1069.

Fureby, C., 2017. Challenges for large Eddy simulation of engineering flows. In: Whither Turbulence and Big Data in the 21st Century? Springer, p. 375–400.

Gad-el-Hak, Pollard, Bonnet, 1998. Flow Control: Fundamentals and Practices. Springer-Verlag, Berlin, Heidelberg.

Gato, L.M.C., Curran, R., 1996. Performance of the contrarotating wells turbine. Int. J. Offshore Polar Eng. 6 (1), 68–75.

Gato, L.M.C., Curran, R., 1997. The energy conversion performance of several types of wells turbine designs. Proc. Inst. Mech. Eng. Part A: J. Power Energy 211 (2), 133–145.

Genc, M.S., Keynak, U., Yapici, H., 2011. Performance of transition model for predicting low re aerofoil flows without/with single and simultaneous blowing and suction. Eur. J. Mech. B/Fluids 30 (2), 218–235.

Georgiadis, N.J., Rizzetta, D.P., Fureby, C., 2010. Large-Eddy simulation: current capabilities, recommended practices, and future research. AIAA J. 48 (8), 1772–1784.

Ghazikhani, M., Khazaee, I., Abdekhodaie, E., 2014. Exergy analysis of gas turbine with air bottoming cycle. Energy 72, 599–607.

Hinze, J.O., 1975. Turbulence. McGraw-Hill Publishing Co., New York.

Hirsch, C., 2007. Numerical Computation of Internal and External Flows: The Fundamentals of Computational Fluid Dynamics. Elsevier Science, Oxford, United Kingdom.

Hitiwadi, M., et al., 2013. Large Eddy simulations of 2D and open-tip airfoils using voxel meshes. Procedia Eng. 61, 32–39.

Hitoshi Hotta, Y.W., 1985. V-5 A study on the matching between the air turbine and phase control for the OWC wave power generator. Ocean Eng. 12 (6), 585–586.

Huang, L., Huang, P.G., LeBeau, R.P., 2004. Numerical study of blowing and suction

control mechanism on NACA0012 airfoil. J. Aircr. 41 (5), 1005–1013.

Iandoli, C.L., 2005. 3-D numerical calculation of the local entropy generation rates in a radial compressor stage. Int. J. Thermodyn. 8, 83–94.

Jubeh, N.M., 2005. Exergy analysis and second law efficiency of a regenerative Brayton cycle with isothermal heat addition. Entropy 7 (3), 172.

Katam, V., 2005. Simulation of Low-Re Flow Over a Modified NACA 4415 Airfoil with Oscillating Camber (Master's thesis). University of Kentucky, Lexington, KY 40506, USA.

Kawai, S., Asada, K., 2013. Wall-modeled large-eddy simulation of high Reynolds number flow around an airfoil near stall condition. Comput. Fluids 85, 105–113.

Kim, K.H., Kim, K., 2012. Exergy analysis of overspray process in gas turbine systems. Energies 5 (12), 2745–2758.

Kim, S.H., Kim, C., 2009. Separation control on NACA23012 using synthetic jet. Aerosp. Sci. Technol. 13 (4), 172–182.

Kim, T.H.. et al., 2002. Hysteretic characteristics of wells turbine for wave power conversion. In: Proceedings of the Twelfth International Offshore and Polar Engineering Conference, The International Society of Offshore and Polar Engineers. Kitakyushu, Japan, p. 687–693.

Kim, T.H., et al., 2002. Numerical investigation on the effect of blade sweep on the performance of wells turbine. Renew. Energy 25, 235–248.

Kim, Y., Castro, I.P., Xie, Z.T., 2015. Large-Eddy Simulations for Wind Turbine Blade: Dynamic Stall and Rotational Augmentation. 20, p. 369–375.

Kinoue, Y., et al., 2003a. Mechanism of hysteretic characteristics of wells turbine for wave power conversion. J. Fluids Eng. 125 (2), 302.

Kinoue, Y., et al., 2003b. Comparison of performances of turbines for wave energy conversion. J. Therm. Sci. 12 (4), 323–328.

Kinoue, Y., et al., 2004. Hysteretic characteristics of monoplane and biplane wells turbine for wave power conversion. Energy Convers. Manag. 45 (9–10), 1617–1629.

Launder, B.E., Spalding, D.B., 1972. Lectures in Mathematical Models of Turbulence. Academic Press, London, England.

Liu, Y., et al., 2012. Numerical simulation of two-dimensional parallel blade-vortex interactions using large Eddy simulation. Procedia Eng. 31, 703–707.

Liu, Z., et al., 2016. Numerical study on a modified impulse turbine for OWC wave energy conversion. Ocean Eng. 111, 533–542.

Lugo-Leyte, R., et al., 2015. Parametric analysis of a two-shaft aeroderivate gas turbine of 11.86 MW. Entropy 17 (8), 5829–5847.

Mamun, M., et al., 2004. Hysteretic flow characteristics of biplane wells turbine. Ocean Eng. 31 (11–12), 1423–1435.

Mamun, M., et al., 2006. Improvement af the performance of the wells turbine by using a very thin elongated endplate at the blade tip. In: Proceedings of the 3rd BSME-ASME International Conference on Thermal Engineering. ASME, Dhaka, Bangladesh.

Mamun, M., 2006. The study on the hysteretic characteristics of the wells turbine in a deep stall condition. In: Energy and Material Science Graduate School of Science and Engineering. Saga University, Japan, p. 141.

Martinat, G., et al., 2008. Turbulence modeling of the flow past a pitching NACA0012 airfoil at 10^5 and 10^6 Reynolds number. J. Fluids Struct. 24, 1294–1303.

Masahiro Inoue, K.K., Setoguchi, Toshiaki, Shimamoto, Katsumi, 1985. II-2 On the starting and quasi-steady characteristics of wells turbine under oscillating flow condition. Ocean Eng. 12 (6), 563.

Masami Suzuki, C.A., Tagori, Tetsuo, 1985. II-4 Fundamental studies on oscillating water column wave power generator with wells turbine. Ocean Eng. 12 (6), 565.

Matos, Ad., Pinho, F.A.A., Silveira!Neto, A., 1999. Large-eddy simulation of turbulent ~ow over a two! Dimensional cavity with temperature ~uctuations. Int. J. Heat Mass Transf. 42, 3848.

Mazzei, L., et al., 2016. Impact of Swirl flow on combustor liner heat transfer and cooling: a numerical investigation with hybrid Reynolds-averaged Navier–Stokes large Eddy simulation models. J. Eng. Gas Turbines Power 138 (5), 051504.

Michioka, T., et al., 2010. Large-Eddy simulation for the mechanism of pollutant removal from a two-dimensional street Canyon. Bound.-Layer Meteorol. 138 (2), 195–213.

Mohamed, M.H., Shaaban, S., 2013. Optimization of blade pitch angle of an axial turbine used for wave rnergy conversion. Energy 56, 229–239.

Moin, P., S.K Cabot, W., Lee, S., 1991. A dynamic subgrid-scale model for compressible turbulence and scalar transport. Phys. Fluids A 3 (11), 2746–2757.

Mortazavi, S.M., Soltani, M.R., Motieyan, H., 2015. A Pareto optimal multi-objective optimization for a horizontal axis wind turbine blade airfoil sections utilizing exergy analysis and neural networks. J. Wind Eng. Ind. Aerodyn. 136, 62–72.

Nomura, T., et al., 2003. Aerodynamic forces on a square cylinder in oscillating flow with mean velocity. J. Wind Eng. Ind. Aerodyn. 91, 199–208.

Okuhara, S., et al., 2013. Wells turbine for wave energy conversion—improvement of the performance by means of impulse turbine for bi-directional flow. Open J. Fluid Dyn. 03 (02), 36–41.

Ozgener, O., Ozgener, L., 2007. Exergy and reliability analysis of wind turbine systems: a case study. Renew. Sustain. Energy Rev. 11 (8), 1811–1826.

Özgökmen, T.M., et al., 2007. Large eddy simulation of stratified mixing in two-dimensional dam-break problem in a rectangular enclosed domain. Ocean Model. 16 (1–2), 106–140.

Pope, K., Dincer, I., Naterer, G.F., 2010. Energy and exergy efficiency comparison of horizontal and vertical axis wind turbines. Renew. Energy 35 (9), 2102–2113.

Pope, S.B., 2004. Ten questions concerning the large-eddy simulation of turbulent flows. New J. Phys. 6 (1), 35.

Raghunathan, S., 1980. Theory and Performance of Wells Turbine. Queen's University of Belfast, Belfast BT7 1NN, United Kingdom, (Rept. WE/80/13R).

Raghunathan, S., 1995a. The wells air turbine for wave energy conversion. Prog. Aerosp. Sci. 31, 335–386.

Raghunathan, S., 1995b. A methodology for wells turbine design for wave energy conversion. ARCHIVE: Proc. Inst. Mech. Eng. Part A: J. Power Energy 1990–1996 (vols. 204–210) 209 (31), 221–232.

Raghunathan, S., Beattie, W.C., 1996. Aerodynamic performance of contra-rotating wells turbine for wave energy conversion. ARCHIVE: Proc. Inst. Mech. Eng. Part A: J. Power Energy 1990–1996 (vols. 204–210) 210 (61), 431–447.

Redha, A.M., Dincer, I, Gadalla, M., 2011. Thermodynamic performance assessment of wind energy systems: an application. Energy 36 (7), 4002–4010.

Rezaei, F., Roohi, E., Pasandideh-Fard, M., 2013. Stall simulation of flow around an airfoil using LES model and comparison of RANS models at low angles of attack. In: Proceedings of the 15th Conference on Fluid Dynamics. The University of Hormozgan, Bandar Abbas, Iran. p. 1–10.

Richards, E.J., Burge, C.H., 1943. An airfoil designed to give laminar flow over the surface with boundary layer suction. Aeronaut. Res. Counc. RM 2263.

Richez, F., et al., 2007. Zonal RANS/LES coupling simulation of a transitional and separated flow around an airfoil near stall. Theor. Comput. Fluid Dyn. 22 (3–4), 305–315.

Rosa, A.Vd., 2012. (ed.)Fundamentals of Renewable Energy Processes Third edition. Elsevier Academic Press, United States of America, 908.

Rosas, C.R., 2005. Numerical Simulation of Flow Separation Control by Oscillator Fluid Injection. A & M University, Texas.

Rumsey, C.L., Nishino, T., 2011. Numerical study comparing RANS and LES approaches on a circulation control airfoil. Int. J. Heat Fluid Flow 32 (5), 847–864.

Saqr, K., 2010. Large eddy simulation: the demand for a universal measure of resolution. CFD Lett., (issres.net).

Saqr, K.M., Wahid, M., Sies, M.M., 2012. Highly-resolved large eddy simulation of the nonreacting flow in an asymmetric vortex combustor. In: Proceedings of the 4th International Meeting of Advances in Thermofluids (IMAT 2011). AIP Publishing.

SB, P., 2000. Turbulent Flows. Cambridge University Press, Cambridge, United Kingdom.

Schatz, M., G¨unther, B., Thiele, F., 2007. Computational investigation of separation control for high-lift airfoil flows. King, P.V.R (ed.), Active Flow Control, Vol. 95. Berlin, Germany. 173–189.

Schlichting, H., 1968. Boundary Layer Theory. McGraw-Hill, New York, USA, 347–362.

Setoguchi, T., et al., 2001. Effect of guide vane shape on the performance of a wells turbine. Renew. Energy 23, 1–15.

Setoguchi, T., et al., 2003a. Effect of rotor geometry on the performance of wells turbine. In: Proceedings of the Thirteenth International Offshore and Polar Engineering Conference. The International Society of Offshore and Polar Engineers, Honolulu, Hawaii, USA, p. 374–381.

Setoguchi, T., et al., 2003b. Hysteretic characteristics of wells turbine for wave power conversion. Renew. Energy 28 (13), 2113–2127.

Setoguchi, T., T.M, Kaneko, K., 1998. Hysteresis on wells turbine characteristics in reciprocating flow. Int. J. Rotat. Mach. 4 (1), 17–24.

Shaaban, S., 2012. Insight analysis of biplane wells turbine performance. Energy Convers. Manag. 59, 50–57.

Shehata, A.S., et al., 2014. Entropy generation due to viscous dissipation around a wells turbine blade: a preliminary numerical study. Energy Procedia 50, 808–816.

Shehata, A.S., et al., 2016. Performance analysis of wells turbine blades using the entropy generation minimization method. Renew. Energy1133–1123 ,86 .

Shehata, A.S., et al., 2017. Comparative analysis of different wave turbine designs based on conditions relevant to northern coast of Egypt. Energy 120, 450–467. http://dx.doi.org/10.1016/j.energy.2016.11.091.

Shehata, A.S., et al., 2017. Wells turbine for wave energy conversion: a review. Int. J. Energy Res. 41 (1), 6–38.

Sheldahl, R.E., Klimas, P.C., 1981. Aerodynamic characteristics of seven symmetrical airfoil sections through 180° angle of attack for use in aerodynamic analysis of vertical axis wind turbines. In: Sandia National Laboratories Energy Report. the United States of America, p. 118.

Skyllingstad, E.D., Wijesekera, H.W., 2004. Large-Eddy simulation of flow over two-dimensional obstacles: high drag states and mixing. J. Phys. Oceanogr. 34, 94–112.

Smagorinsky, J., 1963. General circulation experiments with the primitive equations. I. The basic experiment. Mon. Weak. Rev. 91, 99–164.

Şöhret, Y., et al., 2015. Advanced exergy analysis of an aircraft gas turbine engine: splitting exergy destructions into parts. Energy 90, 1219–1228.

Soltanmohamadi, R., Lakzian, E., 2015. Improved Design of Wells Turbine for Wave Energy Conversion Using Entropy Generation 51. Meccanica, Springer Netherlands, 1713–1722.

Starzmann, R., Carolus, T., 2013. Model-based selection of full-wcale wells turbines for ocean wave energy conversion and prediction of their aerodynamic and acoustic performances. Proc. Inst. Mech. Eng. Part A: J. Power Energy 228 (1), 2–16.

Stodola, A., 1910. Steam and Gas Turbines. McGraw-Hill, New York.

Sue, D.-C., Chuang, C.-C., 2004. Engineering design and exergy analyses for combustion gas turbine based power generation system. Energy 29 (8), 1183–1205.

Takao, M., et al., 2001. The performance of a wells turbine with 3D guide vanes. Int. J. Offshore Polar Eng. 11 (1), 72–76.

Takao, M., et al., 2007. Wells turbine with end plates for wave energy conversion. Ocean Eng. 34 (11–12), 1790–1795.

Tenaud, C., Phuoc, L.T., 1997. Large eddy simulation of unsteady, compressible, separated flow around NACA 0012 airfoil. In: Proceedings of the Fifteenth

International Conference on Numerical Methods in Fluid Dynamics. p. 424–429.

Thakker, A., Abdulhadi, R., 2007. Effect of blade profile on the performance of wells turbine under unidirectional sinusoidal and real sea flow conditions. Int. J. Rotat. Mach. 2007, 1–9.

Thakker, A., Abdulhadi, R., 2008. The performance of wells turbine under bi-directional airflow. Renew. Energy 33 (11), 2467–2474.

Torres, F.R., Teixeira, P.R.F., Didier, E., 2016. Study of the turbine power output of an oscillating water column device by using a hydrodynamic – aerodynamic coupled model. Ocean Eng. 125, 147–154.

Torresi, M., Camporeale, S., Pascazio, G., 2007a. Performance of a small prototype of a high solidity wells turbine. In: Proceedings of the Seventh European Conference on Turbomachinery Fluid Dynamics and Thermodynamics. Athens, Greece.

Torresi, M., Camporeale, S., Pascazio, G., 2007b. Experimental and numerical investigation on the performance of a wells turbine prototype. In: Proceedings of the Seventh European Wave and Tidal Energy Conference. Porto, Portugal.

Torresi, M., Camporeale, S.M., Pascazio, G., 2009. Detailed CFD analysis of the steady flow in a wells turbine under incipient and deep stall conditions. J. Fluids Eng. 131

(7), 071103.

Volino, R.J., Kartuzova, O., Ibrahim, M.B., 2011. Separation control on a very high lift low pressure turbine airfoil using pulsed vortex generator jets. J. Turbomach. 133 (4), 041021.

Walker, S.W., Raymer, W.G., 1946. Wind tunnel test on the 30% symmetrical griffth aerofoil with ejection of air. Aeronaut. Res. Counc. RM 2475.

Whittaker, T.J.T., Stewart, T.P., Curran, R., 1997. Design synthesis of oscillating water column wave energy converters: performance matching. Proc. Inst. Mech. Eng. Part A: J. Power Energy 211 (6), 489–505.

Yagiz, B., Kandil, O., Pehlivanoglu, Y.V., 2012. Drag minimization using active and passive flow control techniques. Aerosp. Sci. Technol. 17 (1), 21–31.

Yousefi, K., Saleh, R., Zahedi, P., 2014. Numerical study of blowing and suction slot geometry optimization on NACA 0012 airfoil. J. Mech. Sci. Technol. 28 (4), 1297–1310.

Yukihisa Washio, H.H., Miyazaki, Takeaki, Masuda, Yoshio, 1985. II-3 Full-scale performance tests on tandem wells turbine. Ocean Eng. 12 (6), 564.